NONTHERMAL RADIATION OF YOUNG SUPERNOVA REMNANTS: THE CASE OF CAS A

V.N.Zirakashvili
Pushkov Institute for Terrestrial Magnetism, Ionosphere and Radiowave Propagation, 142190, Troitsk, Moscow Region, Russia
Max-Planck-Institut für Kernphysik, Saupfercheckweg 1, 69117 Heidelberg, Germany

F.A.Aharonian
Dublin Institute for Advanced Studies, 31 Fitzwilliam Place, Dublin 2, Ireland
Max-Planck-Institut für Kernphysik, Saupfercheckweg 1, 69117 Heidelberg, Germany

R.Yang
Max-Planck-Institut für Kernphysik, Saupfercheckweg 1, 69117 Heidelberg, Germany

E.Oña-Wilhelmi
Max-Planck-Institut für Kernphysik, Saupfercheckweg 1, 69117 Heidelberg, Germany

R.J.Tuffs
Max-Planck-Institut für Kernphysik, Saupfercheckweg 1, 69117 Heidelberg, Germany

ABSTRACT

The processes responsible for the broad-band radiation of the young supernova remnant Cas A are explored using a new code which is designed for a detailed treatment of the diffusive shock acceleration of particles in nonlinear regime. The model is based on spherically symmetric hydrodynamic equations complemented with transport equations for relativistic particles. Electrons, protons and the oxygen ions accelerated by forward and reverse shocks are included in the numerical calculations. We show that the available multi-wavelength observations in the radio, X-ray and gamma-ray bands can be best explained by invoking particle acceleration by both forward and reversed shocks. Although the TeV gamma-ray observations can be interpreted by interactions of both accelerated electrons and protons/ions, the measurements by Fermi LAT at energies below 1 GeV give a tentative preference to the hadronic origin of gamma-rays. Then, the acceleration efficiency in this source, despite the previous claims, should be very high; 25 % of the explosion energy (or approximately $3 \cdot 10^{50}$ erg) should already be converted to cosmic rays, mainly by the forward shock. At the same time, the model calculations do not provide extension of the maximum energy of accelerated protons beyond 100 TeV. In this model, the acceleration of electrons is dominated by the reverse shock; the required 10^{48} erg can be achieved under the assumption that the injection of electrons (positrons) is supported by the radioactive decay of ^{44}Ti.

Subject headings: cosmic rays– acceleration– supernova remnants

1. Introduction

The mechanism of diffusive shock acceleration (DSA) of relativistic particles (Krymsky 1977, Axford et al. 1977, Bell 1978, Blandford & Ostriker 1978) is generally accepted as the most likely paradigm for production of galactic cosmic rays (CR) in supernova remnants (SNRs). Over the last 30 years a significant progress has been achieved in the development of theoretical models and understanding of the basic features of DSA (see e.g. Malkov & Drury 2001, Schure et al. 2012 for a review). On the other hand, the recent detailed studies of spectral and morphological features of young SNRs, first of all in the X-ray and very-high-energy (or TeV) gamma-ray band, provide excellent observational material for development of detailed numerical models of acceleration and radiation of relativistic electrons and protons in young SNRs. These observations generally confirm in general terms the predictions of DSA. In particular the synchrotron X-radiation observed from several young SNRs implies an existence of multi-TeV electrons which is naturally explained by DSA. The detection of TeV gamma-rays from SNRs, like Cas A, RX J1713.7-3946, Vela Jr., RCW 86 (see Hinton & Hofmann 2009; Rieger et al. 2013 for a recent review) give a more direct and unambiguous information about the effective acceleration of particles, electrons and/or protons, in SNRs to energies exceeding 100 TeV.

In this paper we conduct detailed study of acceleration of electrons and protons with an emphasis on the spectral and morphological features of high energy radiation produced by these particles in the young supernova remnant Cas A. For that purpose we use a new numerical code of nonlinear diffusive shock acceleration developed by one of us in collaboration with V. Ptuskin (Zirakashvili & Ptuskin 2012). This model can be considered as a natural development of existing numerical codes (see e.g. Berezhko et al. 1994, Kang et al 2006), with new additional elements which despite their strong impact on the overall picture of acceleration in general, and on the properties of high energy radiation of SNRs in particular, have been ignored in the past. Namely, in our treatment, the solution of spherically symmetric hydrodynamic equations is combined with the transport and acceleration of relativistic particles by the *forward* shock and *reverse* shocks (FS and RS, respectively). The nonlinear response of energetic particles via their pressure gradient results in a self-regulation of acceleration efficiency. The detailed calculations of radio, X-ray, gamma-ray emission components conducted within a self-consistent treatment of the particle acceleration by both forward and reverse shocks should allow a direct comparison of the observed spectral and morphological features with model predictions. The inclusion of the radiation components related to the reverse shock seems to be a rather obligatory condition, at least for the specific case of Cas A. In this regard we note that the parameters that characterize the reverse shock can be significantly different compared to the parameters of the forward shock. Therefore, the properties of radiation components from the reverse and forward shocks are also expected to be significantly different. In particular, the magnetic field in the reverse shock can be very small which would dramatically increase the contribution of the IC component compared to the hadronic (π^0-decay) component of gamma-rays. Because of the stronger magnetic field, in the forward shock just opposite relation is expected between the contributions of electrons and protons to production of high energy gamma-rays.

An interesting feature of Cas A is the non-negligible contribution of the decay of radioactive elements in the ejecta to the production of suprathermal electrons and positrons as a potentially important "injection material". The acceleration of these particles by the reverse shock (Zirakashvili & Aharonian 2011, Ellison et al. 1990) can result in a rather high energy content of leptonic component in SNRs. In particular this can explain the high electron to proton ratio found in Cas A (Atoyan et al. 2000).

The results and conclusion of this study have a rather general character and can be applied to different SNRs. In this paper the model is used to interpret the multi-wavelength properties of Cas A - one of the youngest supernova remnants in our Galaxy. The high quality X-ray images and energy spectra, as well as the coverage of gamma-ray observations from low to very high energies, provide adequate observational material to conduct detailed theoretical studies of acceleration and radiation processes in this unique source.

The paper is organized as follows. In Section

2 we briefly summarize multi-wavelength observations of Cas A. The short description of the model is given in Section 3. The results of modeling of the broad-band emission are presented and discussed in Sections 4, 5, 6 and 7. Finally, in Sections 8 and 9 we discuss and summarize the obtained results.

2. Observational properties of Cas A

The supernova explosion related to Cas A is likely to be linked to the event observed by Flamsteed in 1680 (Ashworth 1980). Recently Krause et al. (2008) reported the detection of its light echo with a spectrum similar to the spectra of IIb supernova 1993J. Therefore one may assume that SNR Cas A was produced in a IIb type supernova explosion. Generally, the progenitors of such explosions are Red Super Giants (RSG) which already have lost their hydrogen envelope via a powerful stellar wind (Chevalier 2005).

Cas A has been extensively observed at radio wavelengths (Bell et al. 1975; Tuffs 1986; Braun et al. 1987; Anderson et al. 1991; Kassim et al. 1995; etc.). The radio spectrum is close to power-law $J(\nu) \sim \nu^{-\alpha}$ with a spectral index $\alpha = 0.77$ (Baars et al. 1977). The main fraction of radio-emission comes from the bright radio-ring with an angular radius close to $100''$ and from the faint outer radio-plateau with an angular radius $150''$. For a distance to the source $D = 3.4$ kpc (Reed et al. 1995), the corresponding spatial radii are 1.7 pc and 2.5 pc, respectively.

In addition to the large-scale structures, several hundreds of very compact and bright radio-knots with steeper spectra (Anderson et al. 1991) are present in the radio-shell. It is believed that the bright radio-ring is related to the reverse shock propagating into the supernova ejecta. A large number of fast-moving knots (FMK) are observed also in optics (e.g. Fesen et al. 1988) are attributed to densest clumps of ejecta which are not strongly decelerated after the supernova explosion. This hypothesis agrees with X-ray observations which show that the X-ray line emitting shell roughly coincides with the bright radio ring. The X-ray emitting plasma is rich in O, Si, Ar, Ca and Fe dominated by the contribution from oxygen (Fabian et al. 1980; Markert et al. 1983; Vink et al. 1996, Hughes et al. 2000; Willingale et al. 2002, 2003; Hwang & Laming 2003; Laming & Hwang 2003).

Besides the line X-ray emission, Cas A shows a hard X-ray continuum extending up to 100 keV with a photon index ~ 3 as measured by *BeppoSAX* (Vink et al. 2001), *INTEGRAL* (Renaud et al. 2006) and *Suzaku* observations (Maeda et al. 2009) satellites. Unfortunately, because of limited angular resolution of these instruments, the production region(s) of the component of radiation cannot be localized. At low energies, thin and faint nonthermal X-ray filamentary structures have been found at the periphery of the remnant close to the boundary of the radio plateau (Gotthelf et al. 2001). These filaments correspond to the position of the forward shock propagating in the circumstellar medium. The proper motion of these filaments has been measured by the *Chandra* observations allowing the estimate of the forward shock velocity of about 4900 km s^{-1} (Patnaude & Fesen 2009).

On the other hand, the inner shell in the radio and X-ray images can be naturally attributed to the reverse shock propagating in the supernova ejecta, assuming that the electrons are accelerated also at the reverse shock (Uchiyama & Aharonian 2008, Helder & Vink 2008). Generally, the reverse shock is not treated as an efficient accelerator, because the magnetic field of ejecta might be very weak due to the large expansion factor of the exploded star. However, similar to the case of the forward shock, the magnetic field can be significantly amplified also at the reverse shock (see Ellison et al. 2005), for example, in the course of the nonresonant streaming instability as suggested by Bell (2004). This implies that we should expect gamma-rays from both forward and reverse shocks the contributions of which however cannot be separated by current gamma-ray telescopes both in GeV and TeV energy bands.

Very high energy gamma-ray emission from Cas A has been discovered by the HEGRA system of atmospheric Cherenkov telescopes (Aharonian et al. 2001), and later confirmed by the MAGIC (Albert et al. 2007) and VERITAS (Acciari et al. 2010) collaborations. The fluxes published by three groups are in a reasonably good agreement with each other, and indicate on a not-very-hard and not-very-soft energy spectrum with a photon index $\gamma = 2.4 - 2.6$ and a maximal energy of detected photons 5 TeV.

At low energies, a weak gamma-rays signal from Cas A has been discovered after the first year of observations with the *Fermi* Gamma-ray Space Telescope (Abdo et al. 2010). While the flux and the energy spectrum reported at energies above 0.5 GeV are quite informative for constraining certain model parameters, they are not sufficient for a robust conclusions concerning, in particular, the origin of radiation. In this regard, the derivation of the energy spectrum at energies below 1 GeV seems to be crucial for identification of the radiation mechanism(s). In particular, a sharp decline of the spectrum below 1 GeV would indicate the dominance of hadronic interactions, at least in this energy band. Motivated by the importance of such spectral measurements, we attempted to reanalyze the *Fermi* LAT data based on much larger statistics accumulated over 4 yr observations, and using the recent *Fermi* LAT software package which allows the extension of the analysis down to 100 MeV. The approach used in this paper for analysis of the *Fermi* LAT data is described in (2012).

We have selected the events with energy between 60 MeV and 100 GeV and applied the usual filters recommended by the *Fermi* LAT collaboration (removing the intervals when the rocking angle of the LAT was greater than 52 deg or when parts of the region-of-interest (ROI) were observed at zenith angles larger than 100 deg). To derive the energy spectrum we applied the maximum likelihood method in 13 independent energy bins from 100 MeV to 100 GeV; the Galactic and isotropic diffuse emission was modeled using the tools *gal-2years7v6-v0* and *iso-p7v6source*. During the broad-band fit, all sources in the second Fermi catalog (2FGL) in the field of view have been included in likelihood model. Points with significance of more than 3σ are shown in Fig. 6, 7,8 and 14. It should be noted that below 200 MeV, the spectrum determination suffers heavily from the background subtraction due to the uncertainties in the model of the Galactic diffuse emission. Applying different models generated by the GALPROP simulator, we obtained a 15 % larger flux that can be account by systematic errors. The obtained spectral energy distribution (SED) shows a significant decrease of the flux below 1 GeV which is expected in the SED of gamma-rays from decays of neutral pions produced at interactions of accelerated protons and nuclei with the ambient gas.

3. Nonlinear model of diffusive shock acceleration

Throughout this paper we use the approach which lies on a nonlinear treatment of particle acceleration by strong shock waves proposed by Zirakashvili & Ptuskin (2012).

Non-steady hydrodynamical equations for the gas density $\rho(r,t)$, gas velocity $u(r,t)$, gas pressure $P_g(r,t)$, and the equation for the quasi-isotropic CR momentum distribution $N(r,t,p)$ in the spherically symmetrical case are solved numerically with the use of a finite-difference method. Thermal protons are injected at the forward shock with a radius $r = R_f(t)$. Since it is believed that the ejecta material in Cas A consists mainly on heavy elements, the oxygen ions are injected at the reverse shock with a radius $r = R_b(t)$[1].

The injection efficiency that is the fraction of particles injected into DSA at the reverse and forward shocks η_b and η_f is taken to be independent of time, and the injection momenta are $p_f = 2m(\dot{R}_f - u(R_f+0,t))$, $p_b = 2M(u(R_b-0,t)-\dot{R}_b)$. Here m and M are the mass of the proton and oxygen ion respectively. We normalize the momentum distribution of oxygen ions N_i to the number density of nucleons. Thus the number density of oxygen ions with atomic mass $A = 16$ is given by $n_i = 4\pi \int p^2 dp N_i/A$.

To obtain the sub-shock compression ratio close to 2.5-2.7, for simulations of cosmic ray modified shocks we adopt the injection efficiency $\eta_b = 0.01$. This is in agreement with calculations of quasi-parallel collisionless shocks (Zirakashvili 2007) and is supported by radio-observations of young extragalactic Ib/c SNRs (Chevalier & Fransson 2006). The amplified magnetic field is rather large in these SNRs and the synchrotron radio-emission is produced by electrons with energies below 1 GeV. The observed radio-flux $J(\nu) \propto \nu^{-1}$ has a power-law dependence on the frequency ν. Note that since the radiative losses of radio electrons are negligible, this corresponds to a E^{-3} type energy spectrum of accelerated electrons. Such a

[1]Throughout the paper we use the subscripts "f" and "b" to the parameters characterizing the forward and reverse (backward) shocks, respectively.

spectrum can be formed at the sub-shock with a compression ratio 2.5.

In older remnants, the magnetic field strength drops and the energy spectra of GeV electrons become flatter due to the higher compression ratio "seen" by these particles. This change of the electron energy distribution is reflected in the spectrum of radio emission

In SNR shells the ion injection may be suppressed at oblique shocks (see Völk et al. (2003) for the discussion of this topic). This can be realized in Cas A where the forward shock propagates in the stellar wind with an azimuthal magnetic field. That is why below we consider two extreme cases with $\eta_f = 0.01$ (hadronic model) and $\eta_f = 10^{-7}$ (leptonic model).

Usually the pressure of energetic electrons is neglected, i.e. the electrons are treated as test particles. However, recently it has been proposed that gamma-rays from the radioactive decay of ^{56}Ni may produce a large number of energetic electrons via Compton scattering in the circumstellar medium. In addition the decays of ^{44}Ti can directly supply energetic electrons and positrons in supernova ejecta (see Zirakashvili & Aharonian 2012 for details). These energetic particles are further accelerated by the forward and reverse shocks. Under these conditions, the reverse shock may be modified by the pressure of electrons (positrons). For this reason in calculations we include the contribution of relativistic electrons to the overall pressure .

The evolution of electron distribution is described by an equation similar to transport equation for protons, but with additional terms describing synchrotron, Coulomb, bremsstrahlung and IC losses. In the scenario of electron injection through the decays of radioactive nuclei ^{56}Ni and ^{44}Ti, the amount of positrons and electrons injected at the forward and reverse shock is described by the injection efficiencies η_f^e and η_b^e respectively. For the forward shock the injection efficiency is determined by the probability of appearance of an energetic electron due to the Compton scattering of gamma-rays from ^{56}Co decay and is given by (Zirakashvili & Aharonian 2011)

$$\eta_f^e = 1.2 \cdot 10^{-7} \frac{M_{\rm Ni}}{M_\odot} r_{\rm pc}^{-2}. \qquad (1)$$

Here $M_{\rm Ni}$ is the mass of ^{56}Ni just after the explosion and $r_{\rm pc}$ is the distance from the center of the remnant expressed in parsecs. ^{56}Co is produced via decay of ^{56}Ni.

For the reverse shock the injection efficiency of electrons and positrons produced directly from the decay of ^{44}Ti can be written as (Zirakashvili & Aharonian 2011)

$$\eta_b^e = 1.94 \frac{M_{Ti}}{44 M_{ej}} \left(1 - \exp\left(-\frac{t \ln 2}{t_{1/2}}\right)\right). \qquad (2)$$

Here M_{ej} is the mass of ejecta, $M_{\rm Ti}$ is the mass of ^{44}Ti just after the explosion, and $t_{1/2} = 63$ yr is the half-time of ^{44}Ti. It was taken into account that one electron and 0.94 positrons appear per a decay of ^{44}Ti.

CR diffusion is determined by magnetic inhomogeneities. Strong streaming of accelerated particles changes medium properties in the shock vicinity. In particular, the CR streaming instability in young SNRs results in a high level of magnetohydrodynamical (MHD) turbulence (Bell 1978) and even in the amplification of magnetic field (Bell 2004). Due to this effect protons can be accelerated to energies beyond the the so-called Lagage and Cesarsky upper limit, $E \sim 100$ TeV (Lagage & Cesarsky 1983).

The magnetic field amplified upstream the shock is enhanced further via compression in the shock transition region. It can even play a dynamical role downstream of the shock. We take magnetic pressure and magnetic energy flux into account downstream of the shock. This is a new element in comparison with the approach of Zirakashvili & Ptuskin (2012) where the magnetic field spatial distribution was prescribed. The magnetic field was transported in the downstream region as the gas with adiabatic index γ_m. Its impact on the shock dynamics was also taken into account via Hugoniot conditions. Upstream of the forward shock where dynamical effects of the magnetic fields are small, the coordinate dependence of the magnetic field B can be prescribed as :

$$B(r) = \sqrt{4\pi\rho_0} \frac{V_f}{M_A^f} \left(\frac{\rho(r)}{\rho_0}\right)^{\gamma_m/2}, \qquad (3)$$

Here ρ_0 and $\rho(r)$ are the undisturbed gas density at the shock position and the density of the

medium where the shock propagates respectively, V_f is the speed of the forward shock. The parameter M_A^f is similar to the Alfvén Much number of the shock and determines the value of the amplified magnetic field strength far upstream of the shock. In the shock transition region the magnetic field strength is increased by a factor of $\sigma^{\gamma_m/2}$, where σ is the shock compression ratio. An expression similar to Eq. (3) is used also in the upstream region of the reverse shock.

Below we use the adiabatic index of isotropic random magnetic field $\gamma_m = 4/3$. For this value of the adiabatic index the magnetic pressure $P_m = B^2/24\pi$ is three times smaller than the magnetic energy density ($= B^2/8\pi$).

CR advective velocity may differ from the gas velocity by the value of the radial component of the Alfvén velocity $V_{Ar} = V_A/\sqrt{3}$ calculated in the isotropic random magnetic field: $w = u + \xi_A V_{Ar}$. The factor ξ_A describes the possible deviation of the cosmic ray drift velocity from the gas velocity. We use values $\xi_A = 1$ and $\xi_A = -1$ upstream of the forward and reverse shocks respectively, where Alfvén waves are generated by the cosmic ray streaming instability and propagate in the corresponding directions. The damping of these waves heats the gas upstream of the shocks (see McKenzie & Völk 1982) and limits the total compression ratios of CR modified shocks. In the downstream region of the forward and reverse shock at $R_b < r < R_f$ we put $\xi_A = 0$ and therefore $w = u$.

We use the diffusion coefficients D_f and D_b at the forward and reverse shocks in the following form

$$D_{f,b} = \eta_B D_B \left(1 + \frac{p}{P_{f,b}}\right), \qquad (4)$$

were $D_B = vpc/3qB$ is the Bohm diffusion coefficient. Since it is expected that the highest energy particles are scattered by small-scale magnetic fields generated in the course of the nonresonant streaming instability, their diffusion coefficient is larger than the Bohm diffusion coefficient and is proportional to p^2 (Dolginov & Toptygin 1967). This effect is described by the second term in parenthesis where P_f and P_b are the momenta which separate these two different regimes of diffusion. The parameter η_B describes the possible deviations of diffusion coefficient from the one achieved in the regime of Bohm diffusion at small energies. It is expected that $\eta_B > 1$ because small energy particles can be resonantly scattered only by a fraction of the magnetic spectrum. Throughout the paper we use the value $\eta_B = 2$. Note that at high energies the particle diffusion is determined by the small-scale magnetic fields, and the values of $P_{f.b}$ in Eq. (4) are adjusted to reproduce the gamma and X-ray observations (see below). Therefore the results of calculations do not strongly depend on the chosen value of $\eta_B = 2$.

In real situations the level of MHD turbulence drops with distance upstream the shock, so the diffusion could be quite fast there. The characteristic diffusive scale of highest energy particles is a small fraction ($\xi_0 << 1$) of the shock radius (see Zirakashvili & Ptuskin 2008), and is determined by the generation and transport of MHD turbulence in the upstream region. The value $\xi_0 \sim \ln^{-1}(D_c/D_s)$ is determined by the ratio of diffusion coefficient D_c in the circumstellar medium and diffusion coefficient $D_s << D_c$ in the vicinity of the shock. The MHD turbulence is amplified exponentially in time before the shock arrival from the background level by the cosmic ray streaming instability. This process is not modeled in the present study; we simply multiply the CR diffusion coefficient D to the additional factor $\exp((r - R_f)/\xi_0 R_f)$ upstream the forward shock and to a similar factor $\exp((R_b - r)/\xi_0 R_b)$ upstream the reverse shock. The characteristic range of variation of ξ_0 is $0.05 \div 0.1$ (Zirakashvili & Ptuskin 2008). Below we use the value $\xi_0 = 0.05$.

In supernova remnants, the plasma is heated to keV temperatures. Generally, in young SNRs the thermal electrons are not in equilibrium with ions. Here we assume that the exchange between electrons and ions proceeds at the minimum rate, i.e. through the Coulomb collisions (Spitzer 1968).

4. Modeling of hydrodynamics and particle acceleration

It is expected that a circumstellar medium around progenitors of IIb supernova is strongly nonuniform. At the main sequence (MS) phase, the stellar wind of progenitor creates a rarefied bubble in the surrounding medium. Later the part of this bubble is filled with a dense gas ejected by progenitor at the Red Super Giant (RSG) phase of the stellar evolution (see Chevalier 2005 for a

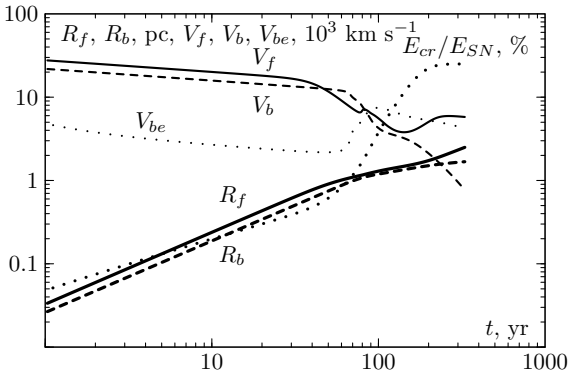

Fig. 1.— Time dependencies of parameters characterizing the forward and reverse shocks: the forward shock radius R_f (thick solid line), the reverse shock radius R_b (thick dashed line), the forward shock speed V_f (thin solid line), the reverse shock speed V_b (thin dashed line), the reverse shock speed in the ejecta frame V_{be} (thin dotted line). The ratio of the energy released in cosmic rays to the total energy of the supernova explosion E_{cr}/E_{SN} (dotted line) is also shown.

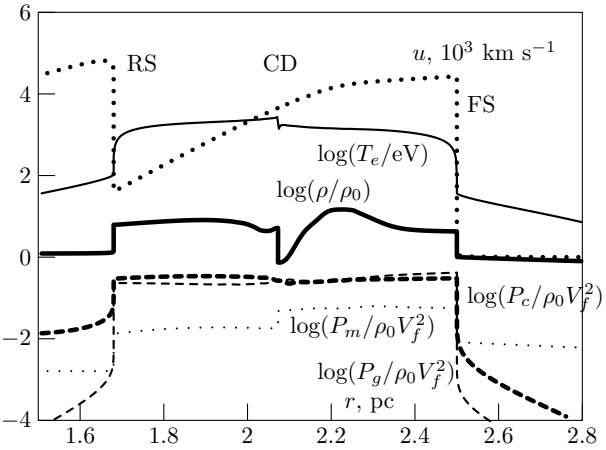

Fig. 2.— Radial dependencies of the gas density (thick solid line), the gas velocity (thick dotted line), the CR pressure (thick dashed line), the gas pressure (dashed line), the magnetic pressure (dotted line) and the electron temperature (solid line) at the epoch $t = 330$ yr. In the same figure the positions of the forward and reverse shocks, (FS and RS, respectively) as well as of the contact discontinuity (CD) are shown.

review). Typically, the progenitors of IIb Supernova are Red-Super Giants (RSG) which have lost almost all hydrogen envelope vie powerful stellar wind with mass-loss rate $\dot{M} = 10^{-5} - 10^{-4}\ M_\odot$ yr^{-1}. It is likely, however, that the progenitor of Cas A prior the explosion had a short Wolf-Rayet or blue supergiant stage. At this stage the progenitor emits a tenuous and fast stellar wind that creates a low density bubble around the progenitor. The fast wind also can compress an inner part of the external slow RSG wind. As a result, a narrow high-density RSG shell is formed at a distance R_s.

For Cas A such a model has been proposed by Chevalier & Liang (1989). It is possible that almost all progenitors of IIb supernova pass through this stage. Since the progenitor of the famous type IIP supernova 1987A also has been in the blue super giant stage, we perhaps can extend this conclusion to other core-collapse supernova progenitors.

The hydrodynamical model with the circumstellar bubble was also considered for Cas A SNR by Borkowsky et al. (1996), by Hwang & Laming (2009) and by Schure et al. (2008).

Stellar evolution models for low mass IIb supernova progenitors (Gregory 2012) do indicate presence of the blue supergiant stage. The blast wave of IIb SNR 1993J has been propagating in the dense RSG wind one decade after explosion and later entered into a low density region (Weiler et al 2007). The main part of the mass lost by the progenitor of 1993J supernova is still outside the SNR shell.

In any case the forward shock of Cas A propagates into the stellar wind. A steady stellar wind has a r^{-2} density profile. The mass density of the stellar wind is given by

$$\rho(r) = \frac{\dot{M}}{4\pi u_w r^2}. \qquad (5)$$

Here u_w and $\dot{M}$ are the speed and mass-loss rate of the stellar wind respectively. For the RSG wind speed we will use the characteristic value of $u_w = 20$ km s^{-1} which agrees with the measured motion of HI absorption features observed in the direction of Cas A (Reynoso et al. 1997). It should be noted that most of measurements show that most of RSGs have lower speeds. However the wind speeds are higher for RSGs with high mass-loss (see Tables 1, 2 of Mauron & Josselin 2011). Since

the forward shock speed is much larger compared to the wind speed, the results depend only on the ratio $\dot{M}/u_w$.

For simplicity we assume that inside the shell at $r < R_s$ the gas density is given by the same Eq. (5) with the ratio $\dot{M}/u_w$ a factor of 100 lower in comparison with the ratio in the outlaying RSG wind. Two regions are separated by the thin gas shell at $r = R_s$ with the mass equal to the mass of the swept up RSG wind. For the numerical modeling we assume that the shell and the transition region have the thickness $0.1R_s$. The actual density distribution is more complex inside the shell (see Schure et al. 2008). However it influences only on the early evolution of SNR when the forward shock propagates in this region. The results obtained at later epochs depend only on the shell radius R_s and the RSG wind density because of the low gas density in the bubble region.

The RSG wind density is poorly constrained by X-ray observations of Cas A. The matter is that most of thermal X-rays are produced in the shocked ejecta gas. In addition the forward shock region shows a significant non-thermal X-ray component. That is why the flux of thermal X-rays and the corresponding amount of the stellar wind gas swept up by the forward shock are rather uncertain in this region.

On the other hand, the ejecta mass estimate $2 - 4\ M_\odot$ (Vink et al. 1996, Willingale et al. 2002, 2003; Hwang & Laming 2003; Laming & Hwang 2003) are rather robust. This range of ejecta masses is also in agreement with stellar evolution models (e.g. Gregory 2012) and the predicted light curves (e.g. Iwamoto 1997) of IIb supernova. We shall use the lower limit of ejecta mass $M_{ej} = 2M_\odot$ below.

In this study we use the solar composition for the stellar wind material. The corresponding number density of helium nuclei is $0.1n_H$ where n_H is the undisturbed number density of hydrogen ions at the current forward shock position. So the total nucleon density is $n = 1.4n_H$.

The principal parameters used in calculations are summarized in Table 1 and Table 2. Both tables consist of three parts (separated by vertical lines). The first parts contain general parameters that are fixed for all model calculations. The second parts contain free parameters which are adjusted to match the key observations. The third parts contain the results derived from modeling.

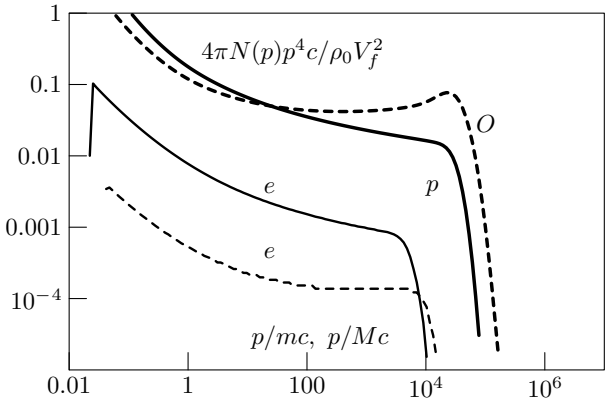

Fig. 3.— The energy distributions of protons at the forward shock (thick line), of oxygen ions at reverse shock (thick dashed line), of electrons at the forward shock (multiplied to the factor of 10^2, thin lines) and of electrons at the reverse shock (thin dashed line) calculated for the model H1 at the epoch $t = 330$ yr. Particle momenta are normalized to the proton mass m and the mass of oxygen ion M. The oxygen spectrum is normalized to the nucleon number density.

4.1. Hadronic models

For hadronic model H1 we use high injection efficiencies $\eta_f = \eta_b = 0.01$ at forward and reverse shocks. The stellar wind density n_H is then adjusted to reproduce the fluxes of gamma-emission. The explosion energy is adjusted to reproduce the forward shock radius $R_f = 2.5$ pc at the remnant age $t = 330$ yr. The value of the amplified magnetic field is parameterized by the parameters $M_A^f = 4.5$ and $M_A^b = 8$ at forward and reverse shocks respectively. These numbers regulates the shape of particle spectra and the corresponding spectra of gamma-emission.

We found that in this model with a rather low stellar wind density, $n_H = 0.4$ cm^{-3}, the amount of suprathermal electrons produced via Compton scattering of gamma-rays from ^{56}Co decay is not sufficient for explanation of the observed radio fluxes. Therefore, in this model it is assumed that the injection of electrons at the forward shock is similar to the injection of protons.

Table 1: Simulated models of Cas A

model	$M_{ej}{}^a$	$k_{ej}{}^b$	$R_f{}^c$	D^d	$R_s{}^e$	$M_A^{f\,f}$	$M_A^{b\,g}$	$n_H{}^h$	$E_{SN}{}^i$	$n_{ej}{}^j$	$R_b{}^k$	$R_c{}^l$	$V_f{}^m$	$V_b{}^n$	$V_{be}{}^o$	$B_f{}^p$	$B_b{}^q$
H1	2.0	9	2.5	3.4	1.5	4.5	8	0.40	1.2	0.69	1.68	2.07	5.8	0.77	4.2	1.16	0.57
H2	2.0	9	2.5	3.4	0	5	5	0.36	1.2	0.67	1.82	1.90	6.0	4.0	1.4	1.0	0.27
L1	2.0	9	2.5	3.4	0	10	10	1.0	2.0	0.30	1.64	1.74	5.7	3.1	1.8	0.78	0.12

[a] mass of ejecta, solar masses
[b] power-law index of ejecta density distribution
[c] forward shock radius, pc
[d] distance to SNR, kpc
[e] RSG shell radius, pc
[f] parameter of magnetic amplification at the forward shock
[g] parameter of magnetic amplification at the reverse shock
[h] undisturbed hydrogen number density at the forward shock position, cm^{-3}
[i] explosion energy, 10^{51} erg
[j] number density of unshocked ejecta, nucleons cm^{-3}
[k] reverse shock radius, pc
[l] radius of the contact discontinuity, pc
[m] forward shock speed, 10^3 km s^{-1}
[n] reverse shock speed in the laboratory frame, 10^3 km s^{-1}
[o] reverse shock speed in the ejecta frame, 10^3 km s^{-1}
[p] magnetic field just downstream of the forward shock, mG
[q] magnetic field just downstream of the reverse shock, mG

On the other hand the amount of electrons (positrons) from the decays of ^{44}Ti is sufficient for production of radio flux of the reverse shock. In calculations we adopted the mass of ^{44}Ti found in observations of Cas A $M_{\mathrm{Ti}} = 1.6 \cdot 10^{-4} M_\odot$ (Renaud et al. 2006).

The electron injection efficiency at the forward shock η_f^e and the injection momentum 40 MeV/c of electrons (positrons) at the reverse shock were adjusted to reproduce the radiofluxes of the shocks.

Figures 1-7 and 9-13 illustrate the numerical results obtained in the hadronic scenario.

The time evolution of the shock radii R_f and R_b, the forward and reverse shock speeds $V_f = \dot{R}_f$ and $V_b = \dot{R}_b$, the reverse shock speed in the ejecta frame $V_{be} = R_b/t - \dot{R}_b$ and the ratio of CR energy to the energy of supernova explosion E_{cr}/E_{SN} are shown in Fig.1.

At early times after SN explosion the ratio of forward and reverse shock radii is independent on time. Approximately after 40 years after the explosion, the forward shock starts to interact with the dense gas of the RSG shell, the speeds of both shocks drop and the distance between shocks decreases. At 150 years after explosion the forward shock leaves the shell and enters into undisturbed RSG wind. At this time the forward shock swept up the gas mass $\sim 1.6 M_\odot$ comparable to the ejecta mass and the transition to the Sedov phase began. At present the forward shock speed is $V_f = 5.8 \cdot 10^3$ km s^{-1} that is 15% higher than the measured proper motion $\sim 5.0 \cdot 10^3$ km s^{-1} of the X-ray filaments (Patnaude & Fesen 2009).

The reverse shock position $R_b = 1.68$ pc is at the upper boundary of observed values $1.5 \div 1.7$ pc. For higher ejecta mass $M_{ej} > 2 M_\odot$ the reverse shock is shifted to larger radii in contradiction with observations. The reverse shock speed $V_b = 0.77 \cdot 10^3$ km s^{-1} is in agreement with measured in radio speed $(1.16 \pm 0.50) \cdot 10^3$ km s^{-1} (Delaney & Rudnick 2003) and is lower than measured in optics speed $3 \cdot 10^3$ km s^{-1} (Morse et al. 2004).

Radial dependencies of several key parameters at the present epoch $t = 330$ yr are shown in Fig.2. In the same figure we show the positions of the contact discontinuity and the forward and reverse

Table 2: Details of particle acceleration

model	η_f [a]	η_b [b]	η_b^{ec}	η_f^{ed}	P_f [e]	P_b [f]	p_f^{eg}	p_b^{eh}	K_{en}^{fi}	K_{en}^{bj}	E_{CR}/E_{SN} [k]	σ_f [l]	σ_b [m]
H1	0.01	0.01	$3.5 \cdot 10^{-6}$	$2.2 \cdot 10^{-6}$	0.94	9.4	p_f	40	$4 \cdot 10^{-4}$	0.004	0.25	4.3	4.9
H2	0.01	0.01	$3.5 \cdot 10^{-6}$	$2.5 \cdot 10^{-6}$	∞	∞	p_f	90	$5 \cdot 10^{-4}$	0.18	0.18	4.4	4.4
L1	10^{-7}	0.01	$3.5 \cdot 10^{-6}$	$4.0 \cdot 10^{-9}$	∞	∞	200	200	0.25	0.73	$3 \cdot 10^{-3}$	4.0	5.5

[a] injection rate of protons at the forward shock
[b] injection rate of oxygen ions at the reverse shock
[c] injection rate of electrons (positrons) at the reverse shock at present epoch, see Eq. (2)
[d] injection rate of electrons at the forward shock, for the model L1 see Eq. (1)
[e] momentum that separates two regimes of diffusion at the forward shock, TeV/c, see Eq. (4)
[f] momentum that separates two regimes of diffusion at the reverse shock, TeV/c, see Eq. (4)
[g] injection momentum of electrons at the forward shock, MeV/c
[h] injection momentum of electrons at the reverse shock, MeV/c
[i] electron to proton ratio at the forward shock calculated for the energy 10 GeV
[j] electron to nucleon ratio at the reverse shock calculated for the energy 10 GeV
[k] ratio of cosmic ray energy E_{CR} to the energy of supernova explosion E_{SN}
[l] total compression ratio of the forward shock
[m] total compression ratio of the reverse shock

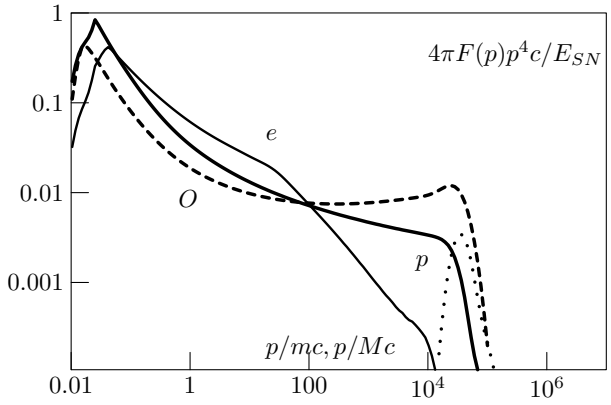

Fig. 4.— Spatially integrated spectra of accelerated protons (solid line), oxygen ions (dashed line) and electrons multiplied to 10^3 (thin solid line) at $t = 330$ yr obtained in the model H1. Spectrum of run-away protons which have left the remnant is also shown (dotted line).

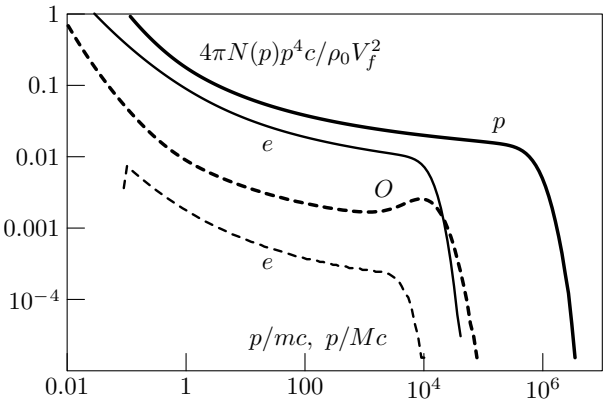

Fig. 5.— The energy distributions of protons at the forward shock (thick line), of oxygen ions at the reverse shock (thick dashed line), of electrons at the forward shock multiplied to 10^3 (thin lines) and of electrons at the reverse shock (thin dashed line) calculated for the model H2 at the epoch $t = 330$ yr. Particle momenta are normalized to the proton mass m and the mass of oxygen ion M. The oxygen spectrum is normalized to the nucleon number density.

shocks. CR, gas and magnetic pressures at the forward shock are 30%, 42% and 6% of the ram pressure $\rho_0 V_f^2$, respectively. At present the forward shock have swept up $2.7 M_\odot$ of the stellar wind material. The reverse shock have swept up $1.66 M_\odot$ of ejecta while $0.34 M_\odot$ of ejecta is not shocked yet.

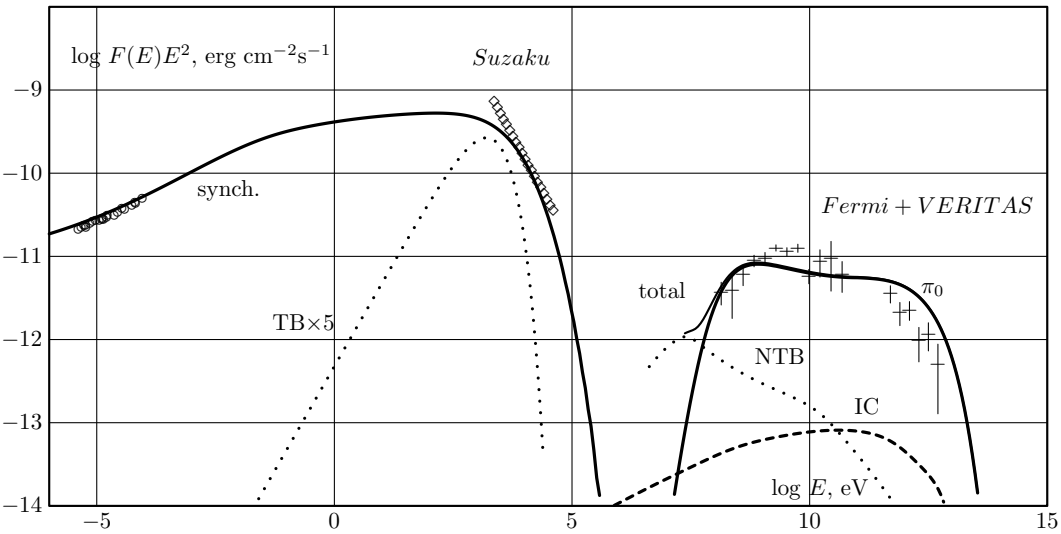

Fig. 6.— The broad-band spectral energy distribution of nonthermal radiation of Cas A calculated within the hadronic model H1. The following radiation processes are taken into account: synchrotron radiation of accelerated electrons (solid curve on the left), IC emission (dashed line), gamma-ray emission from pion decay (solid line on the right), thermal bremsstrahlung (dotted line on the left), nonthermal bremsstrahlung (dotted line on the right). Experimental data in gamma-ray (Fermi LAT, present work); VERITAS, Acciari et al. 2010, data with error-bars) and radio-bands (Baars 1977, circles), as well as the power-law approximation of Suzaku X-ray data (Maeda et al. 2009, diamonds) from the whole remnant are also shown.

The minimal electron heating by Coulomb collisions still results in rather high electron temperatures. The shocked ejecta and the shocked stellar wind plasma are heated up to 2.0 keV and 1.4 keV respectively.

It should be noted that our one-dimensional calculations cannot adequately describe the development of the Rayleigh-Taylor instability of the contact discontinuity. In real situations the supernova ejecta and the circumstellar gas are mixed by turbulent motions in this region (see e.g. MHD modeling of Jun & Norman 1996).

Spectra of accelerated protons, the oxygen ions and electrons are shown in Fig.3. At the present epoch the maximum energy of protons accelerated in this SNR and still confined in the shell, is about 40 TeV; the higher energy protons have already left the remnant.

Spatially integrated proton and electron spectra at the present epoch $t = 330$ yr are shown in Fig.4. We also show the spectrum of run-away particles. These particles have already left the acceleration site through an absorbing boundary at $r = 1.2R_f$. The sum of the proton spectra shown is the total cosmic ray spectrum produced in this SNR over the last 330 years after SN explosion. For this SNR, the spectrum of cosmic ray protons have a maximum energy about 60 TeV that is lower than the knee in the observable cosmic ray spectrum.

To demonstrate the influence of the enhanced diffusion and RSG shell we consider also the hadronic model H2 with the parameters similar to the parameters of the model H1 but without RSG shell and with Bohm diffusion ($P_{f,b} = \infty$, see Tables 1,2). Spectra of accelerated protons, oxygen ions and electrons are shown in Fig.5. In this model with slower diffusion the maximum energy of the protons accelerated is close to 1 PeV.

4.2. Leptonic model

In leptonic models of gamma-ray emission, protons play negligible role in the forward shock dynamics and in the production of electromagnetic emission. Therefore we use rather low injection efficiency $\eta_b = 10^{-7}$ of protons at the forward shock. This very low injection efficiency is possible because the forward shock propagates in the stellar

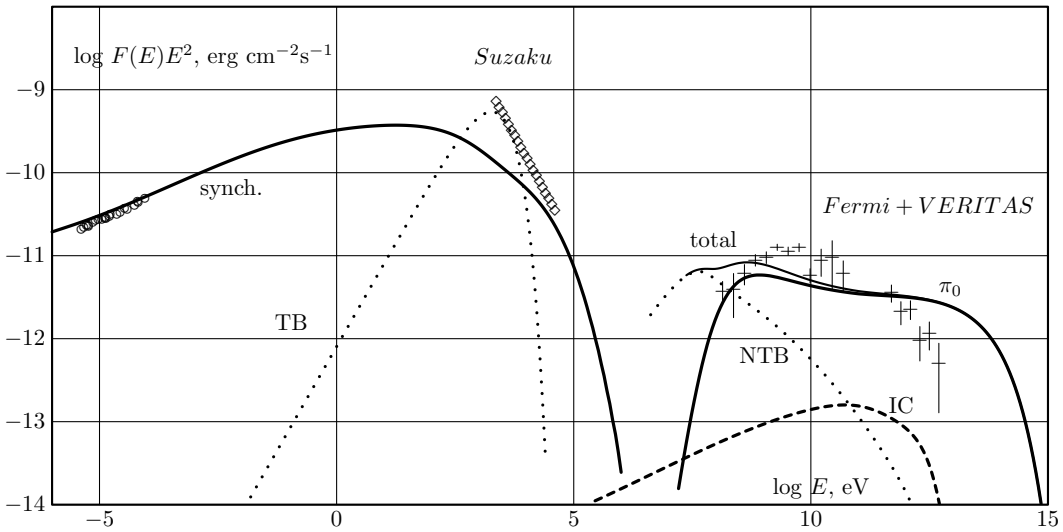

Fig. 7.— The broad-band spectral energy distribution of nonthermal radiation of Cas A calculated for the hadronic model H2. The following radiation processes are taken into account: synchrotron radiation of accelerated electrons (solid curve on the left), IC emission (dashed line), gamma-ray emission from pion decay (solid line on the right), thermal bremsstrahlung (dotted line on the left), nonthermal bremsstrahlung (dotted line on the right). The detected spectral points in the gamma-ray (*Fermi* LAT, this work; VERITAS, Acciari et al. 2010) and radio bands (Baars 1977, circles), as well as the power-law approximation of the Suzaku X-ray data (Maeda et al. 2009, diamonds) from the whole remnant are also shown.

wind with the azimuthal magnetic field. The magnetic field amplification here can't be produced by accelerated particles. It is probably due to vortex motions which are created downstream of the shock in the course of an interaction of stellar wind density fluctuations with the shock front (see Giacalone & Jokipii 2007).

In this model with a rather high stellar wind density $n_H = 1.0$ cm^{-3} the amount of suprathermal electrons generated in the stellar wind gas by the Compton scattering of gamma-rays from ^{56}Co decay is enough for the electron injection at the forward shock.

The electron injection efficiencies correspond to the realistic mass of ^{56}Ni $M_{\rm Ni} = 0.2 M_\odot$ and to the ^{44}Ti mass $M_{\rm Ti} = 1.6 \cdot 10^{-4} M_\odot$ revealed by observations of Cas A (Renaud et al. 2006). The injection momenta 200 MeV/c of electrons from IC scattered gamma-rays at the forward shock and directly from ^{44}Ti decays at the reverse shock are adjusted to reproduce radio, X-ray and gamma-ray fluxes. Since the electrons and gamma-rays from radioactive decays are produced with small energies, a significant increase of their energy up to $E \sim 200$ MeV is required. It can be realized through a stochastic mechanism of acceleration in highly turbulent upstream regions of the reverse and forward shocks (Zirakashvili & Aharonian 2011). The pressure of electrons and positrons at the reverse shock could be comparable to the pressure of ions. Therefore the reverse shock can be significantly modified due to the total pressure of ions and relativistic electrons.

5. Modeling of radiation

In this section we present the results of numerical calculations of radiation produced in interactions of accelerated electrons and protons. The gamma-ray spectra from proton-proton interactions are calculated using the formalism of Kelner et al. (2006). Since π^0-decay gamma rays from the reverse shock are produced mainly in oxygen-oxygen collisions, we use the following approximation. The gamma-ray flux produced by energetic nuclei is given by the gamma-ray flux produced by energetic protons with a number density equal to the nucleon number density of energetic nuclei. The target medium with a mixed composition

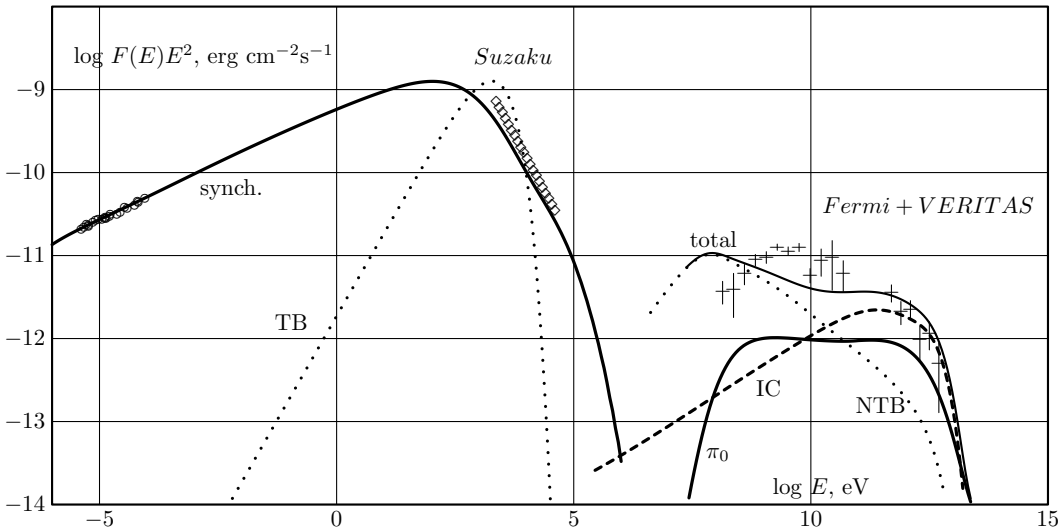

Fig. 8.— The broad-band spectral energy distribution of Cas A calculated for the leptonic model of gamma-ray emission (model L1). The following radiation processes are taken into account: synchrotron radiation of accelerated electrons (solid curve on the left), IC emission (dashed line), π^0-decay gamma-ray emission (solid line on the right), thermal bremsstrahlung (dotted line on the left), nonthermal bremsstrahlung (dotted line on the right). The detected spectral points in the gamma-ray (*Fermi* LAT, this work; VERITAS, Acciari et al. 2010) and radio bands (Baars 1977, circles), as well as the power-law approximation of the Suzaku X-ray data (Maeda et al. 2009, diamonds) from the whole remnant are also shown.

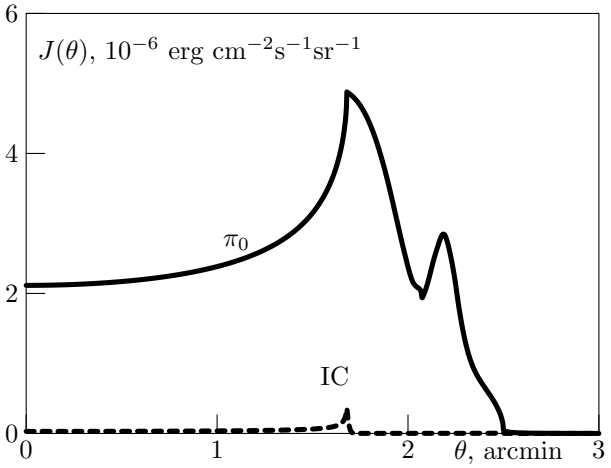

Fig. 9.— Radial profiles of 1 TeV gamma-rays in hadronic model H1: π_0-decay gamma-rays (solid line), IC gamma-rays (dashed line). Gamma-emission from nonthermal bremsstrahlung is very small; its contribution is not shown.

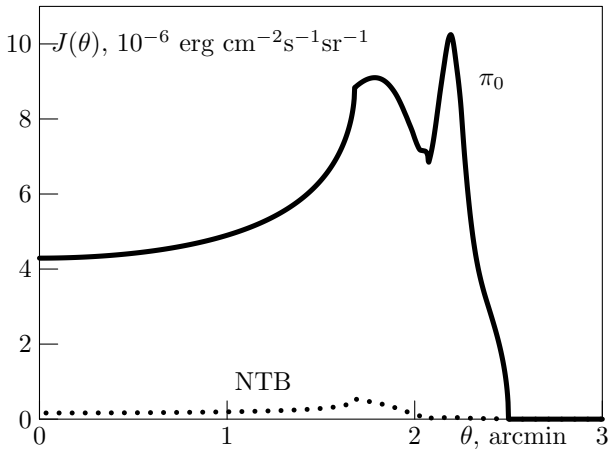

Fig. 10.— Radial profiles of 1 GeV gamma-rays in hadronic model H1: π_0-decay gamma-rays (solid line), gamma-rays from nonthermal bremsstrahlung (dotted line). The contribution of IC gamma-ray emission is negligible.

is substituted by a pure hydrogen plasma with a number density equal to the number density of nucleons in plasma with a mixed composition. For heavy nuclei this approximation slightly overestimate the flux of gamma-emission. This was taking into account using the calculations of the nuclear enhancement factor of Mori (2009). For oxygen-oxygen collisions this gives the correction factor 0.6.

For IC gamma-rays we use the standard expressions of cross-sections (see e.g. Blumenthal & Gould 1970). The main the target photons contributing to the gamma-ray production are the microwave background radiation and the infra-red emission of Cas A itself, with the energy density 2 eV cm^{-3} and temperature $T = 200$ K. The contributions of other diffuse radiation fields can be neglected. For calculations of synchrotron radiation we take into account that in highly turbulent regions close to the inverse and forward shocks, the magnetic field has some probability distribution $P(B)$. This makes the cut-off in the spectrum of synchrotron radiation somewhat smoother (Zirakashvili & Aharonian 2010, see also Bykov et al. 2008).

The results of calculations of the broad-band emission for the hadronic scenario H1 are shown in Fig.6. The principal model parameters used in calculations are described in Table 1 and Table 2. Note that at the present epoch, 25 % of the explosion energy ($E_{SN} = 1.2 \times 10^{51}$ erg) has been transferred to accelerated particles (see Fig.1), most of which are still confined in the shell of the remnant (see Fig.4).

At low energies, the spectra of accelerated particles at CR modified shocks become softer which may results in a significant spectral steepening of synchrotron radio emission.

The contribution of electrons directly accelerated by the reverse shock to synchrotron radiation and IC gamma-rays is significant. In particular, the reverse shock produces 50% of radio and 90% of 5 keV synchrotron X-rays.

In this model gamma-rays are produced mainly via pion decay downstream of the forward and reverse shock (equal contributions at 1 TeV). The modeled gamma-ray flux is slightly above the data at high energies beyond 1 TeV. A better agreement with data can be achieved for smaller values of the parameter $\xi_0 < 0.05$.

In Fig.6 we show also the energy flux of the thermal bremsstrahlung. It is known that the thermal X-rays of Cas A are produced mainly in the dense knots of supernova ejecta. To take this effect into account and to explain soft X-ray data we multiply the X-ray thermal bremsstrahlung flux on the factor of $\xi_X = 5$. This means that the volume factor of the X-ray emitting plasma is below 0.2. The flux of non-thermal X-rays is about 70% of the total X-ray flux at 5 keV.

The results of calculations of the broad-band emission for hadronic model H2 are shown in Fig.7.

In this model the ejecta gas is compressed into the thin shell downstream of the reverse shock. The thermal bremsstrahlung from this shell makes the main X-ray contribution at energies below 10 keV. At higher energies the synchrotron X-rays from the forward shock dominate in X-ray spectrum. The reverse shock produces only 12% of non-thermal X-rays. The calculated gamma-ray emission is produced mainly at the forward shock and is above the data points at high energies above 1 TeV. The same is true at low energies below 1 GeV where the non-thermal bremsstrahlung of electrons accelerated at the reverse shock gives a non-negligible contribution. The shocks produce equal amount of radio-emission.

The results of calculations of the broad-band emission for leptonic scenario are shown in Fig.8.

The reverse shock produces 40% of radio and 50% of 5 keV X-rays. The radio-spectrum of the non-modified forward shock is rather steep. This is because the electrons were mainly injected and accelerated at early stages of the remnant expansion (see Eq.(1)) when the synchrotron losses result in the steepening of electron energy distribution.

In this model gamma-rays are produced mainly by non-thermal bremsstrahlung and IC scattering at the reverse shock. The modeled gamma-ray flux is in good agreement with observations at high energies but is significantly higher than Fermi LAT data below 1 GeV.

6. Radial profiles

The radial profiles of brightness distributions of X-ray, gamma-ray and radio- emissions calculated for the hadronic model H1 are shown in Fig.9-11. The projection effect is taken into account.

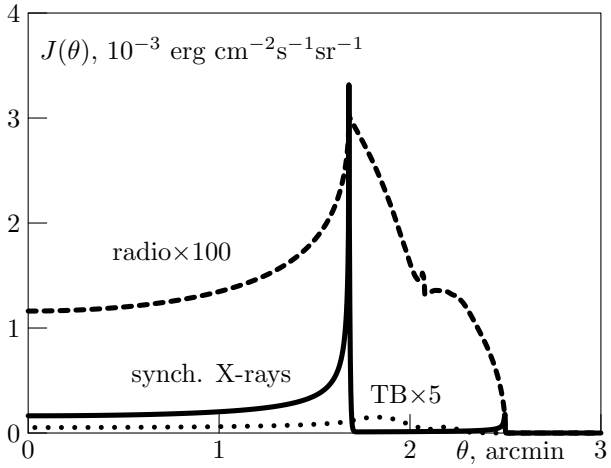

Fig. 11.— Profiles of 5 keV X-rays in the hadronic model H1: synchrotron X-rays (solid line), thermal bremsstrahlung X-rays (multiplied to the factor of 5; dotted line). Radio-brightness at 1.4 GHz multiplied to the factor of 100 is also shown (dashed line).

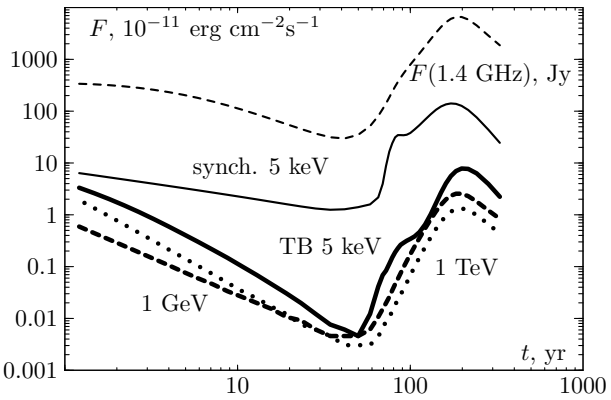

Fig. 12.— Time dependence of fluxes of electromagnetic radiation in the hadronic model H1: 5 keV thermal bremsstrahlung (thick solid line), 5 keV synchrotron X-rays (thin solid line), 1 GeV gamma-emission (thick dashed line), 1 TeV gamma-emission (dotted line); radio at 1400 MHz (thin dashed line).

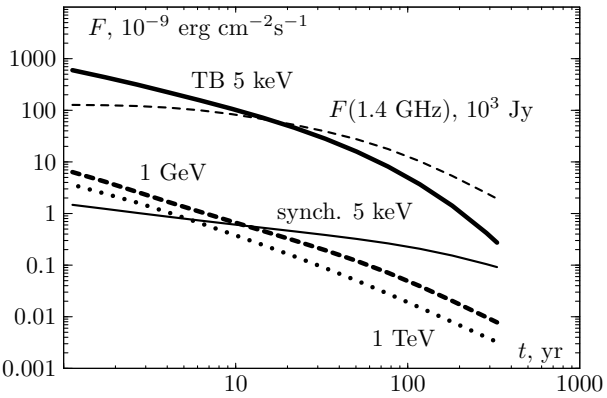

Fig. 13.— Time dependence of fluxes of electromagnetic radiation in the hadronic model H2: 5 keV thermal bremsstrahlung (thick solid line), 5 keV synchrotron X-rays (thin solid line) 1 GeV gamma-emission (thick dashed line), 1 TeV gamma-emission (dotted line); radio at 1400 MHz (thin dashed line).

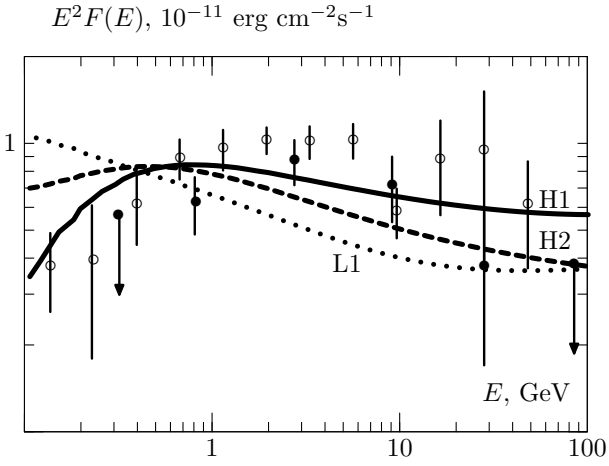

Fig. 14.— Gamma-ray fluxes calculated within the frameworks of the models H1 (solid line), H2 (dashed line) and L1 (dotted line). For comparison the fluxes detected by the *Fermi* LAT are shown. Filled circles - spectral points reported by the Fermi collaboration (Abdo et al. 2010), open circles - the results of our analysis of the *Fermi* LAT data.

All three components of radiation in the radio, X-ray and gamma-ray bands peak at the contact discontinuity and at the reverse shock (approximately $1.7 - 2.0'$ of the angular radius).

The narrow peak of gamma-emission at angular radii $\theta > 2'$ (see Figures 9 and 10) is produced by the forward shock protons in the gas of the RSG shell swept up by the forward shock.

The radio and X-ray profiles in Fig.11 are in agreement with available observations (Anderson et al. 1991, Gotthelf et al. 2001, Helder & Vink 2008).

The sharpest features in the radial profiles appear in X-rays (see Fig.11). Such sharp features imply filamentary structures at forward and reverse shocks. Note that the projection effect works differently for reverse shock in comparison with the forward shock (see Zirakashvili & Aharonian 2010). As a result, the filaments look similar in spite of a relatively weak magnetic field at the reverse shock.

The calculated width of filaments shown in Fig.11 is close to $1''$ which is slightly less than the thickness measured by *Chandra* (Bamba et al. 2004). It has been argued by Völk et al. (2005) that the observed thickness corresponds to the downstream magnetic field of about 500 μG. The larger fields demanded by our model results in narrower filaments. The observed broader filaments can be explained by the limited angular resolution and/or by inhomogeneous circumstellar medium.

In realistic scenarios, the corrugated shock surfaces and the development of Rayleigh-Taylor instability near the contact discontinuity will destroy a picture of ideal circle filaments. Nevertheless, non-thermal X-ray filaments must be observed in the reverse shock region in Cas A.

The dominance of ejecta in thermal X-rays is not surprising since Cas A is at transition from the ejecta dominated stage to Sedov stage now. It is well established that thermal X-rays from very young extragalactic supernova are produced by a shocked ejecta gas (see e.g. Chevalier & Fransson 2006).

7. Secular evolution of fluxes

The calculated temporal dependencies of radiation fluxes in radio, X-ray, and gamma-ray bands in the hadronic models H1 and H2 is shown in Fig.12 and 13. Results for epochs $t < 30$ yr shown in Fig. 12 can be used also for Ib/c SNRs with tenuous winds of Wolf-Rayet stars. Results for H2 model (Fig. 13) are more appropriate for IIb SNRs with dense RSG stellar wind. The rate of the secular decrease of electromagnetic radiation calculated for these two hadronic models, as well as for the leptonic model, are summarized in Table 3.

The rates of decrease of GeV and TeV gamma-ray flux predicted by hadronic models are significantly larger than the one expected in the leptonic model. It should be noted that since the radiation field of Cas A is dominated by its own infra-red radiation, the secular decrease of inverse Compton gamma-rays is affected by the decrease of the density of the target field. For simplicity, the decrease rate of IC gamma-rays 0.12% yr^{-1} in Table 3 has been calculated assuming a time-independent radiation field. Therefore the secular decrease of IC gamma-rays should be somewhat faster given the secular evolution of the infra-red radiation, but still it remains significantly slower than the decrease of gamma-ray flux in hadronic models.

The current secular decrease of radio-intensity 0.85% yr^{-1} is close to measurements of Baars et al. (1977) (0.93$\pm$0.05% yr^{-1} at 1.4 GHz) and higher than measurements of O'Sullivan & Green (1999) (0.6% yr^{-1} at 15 GHz). At the same time, the calculated rates of decrease of 5 keV X-ray fluxes predicted by hadronic and leptonic models close to 1% per year is slower than the measured value (1.5 ± 0.17)% yr^{-1} (Patnaude et al. 2011).

The fast decrease of radio and X-ray emissions in the models H1 and L1 is explained by the significant contribution of the reverse shock to the radio and X-ray production. Presently, it propagates through the flat part of the ejecta spatial density distribution. The ejecta density ρ_{ej} drops proportional to t^{-3}, i.e, 0.9% per year. The fast drop is the main factor which determines the decrease of thermal and nonthermal X-rays.

Since the synchrotron X-rays are produced in the loss-dominated regime the X-ray flux $F(E)$ of the reverse shock can be written as

$$F(E) \propto E^{-2} \rho_{ej} V_{be}^3 R_b^2 f(E/E_0) \qquad (6)$$

where E_0 is the maximum energy of synchrotron

X-rays and the function $f(x)$ describes the shape of the spectral synchrotron cut-off (see also Patnaude et al. 2011). It is also assumed that the the electron energy density is proportional to the ram pressure of the shock $\rho_{ej}V_{be}^2$. For the energy E_0 which is proportional to the square of the shock speed V_{be} , we can estimate the secular decrease of X-ray flux as

$$\frac{\dot{F}}{F} = \frac{\dot{\rho}_{ej}}{\rho_{ej}} + (2\Gamma_X - 1)\frac{\dot{V}_{be}}{V_{be}} + 2\frac{\dot{R}_b}{R_b} \qquad (7)$$

Here Γ_X is the spectral slope $\Gamma_X = -d\ln F/d\ln E$. Using dependencies $V_{be} \sim t^{-0.6}$, $R_b \sim t^{0.2}$ (see Fig.1) and the observational value $\Gamma_X = 3$ we obtain $F \sim t^{-5.6}$ that is the secular decrease 1.7% yr^{-1}. The total secular decrease of X-rays is lower because the thermal X-rays and the forward shock give an additional contribution. The X-ray flux of the forward shock decreases slower because in the stellar wind the density at the forward shock $\rho_0 R_f^2 =$ const. That is why the decrease of synchrotron X-rays at the forward shock depends only on the decrease of the forward shock speed. Then the equation similar to Eq. (7) gives the synchrotron flux decrease proportional to V_f^5. For the measured dependence $V_f \sim t^{-0.2}$, we obtain the secular decrease at the forward shock of order of 0.3% yr^{-1}.

This is demonstrated in Fig. 13 for the H2 model in which the non-thermal X-rays are produced at the forward shock.

In this regard the fast decrease ($> 1\%$ yr^{-1}) of hard X-ray flux reported by Patnaude et al. (2011) is in favor of the interaction with the RSG shell in past (model H1). During this interaction the reverse shock speed V_{be} increases significantly, but presently this speed decreases (see Fig.1). This results in the secular decrease of the non-thermal X-ray flux from the reverse shock that is faster than secular decrease of the ejecta density 0.9% yr^{-1}. The situation is different in the models without RSG shell (H2, L1). In these models, the speed V_{be} presently is almost constant. Correspondingly, the secular decrease of the nonthermal X-ray flux cannot be faster than 0.9% yr^{-1}.

We conclude that the model H1 is in better agreement with the measured secular decrease, although for X-rays even the model H1 predicts slower decrease than the observations show.

We may directly compare the results of our calculations with radio-observations of well-studied extragalactic IIb supernova 1993J (Weiler et al. 2007). Its radio flux at $\lambda = 20$ cm was ~ 30 mJy at day 3000. This corresponds to ~ 30 kJy recalculated for Cas A distance which is a factor of 3 smaller than the value corresponding to the radio-curve in hadronic model H2 (see Fig.13). The reason could be that in Cas A the electron injection is more efficient in Cas A than in SNR 1993J or it was lower in past.

The model H2 predicts gamma-ray flux one year after the explosion at the level of 10^{-8} erg cm^{-2}s^{-1}. This corresponds to the flux $\sim 10^{-14}$ erg cm^{-2}s^{-1} recalculated for SNR 1993J distance. This estimate agrees with the results of Tatischeff (2009), but is below by two orders of magnitude the flux predicted by Kirk et al. (1995). The reason of such a large discrepancy is the higher wind density assumed by Kirk et al. (1995).

8. Discussion

8.1. Circumstellar medium around Cas A

According to the recent proper motion X-ray measurements (Patnaude & Fesen 2009), the expansion parameter of Cas A is $m_{exp} = V_f t/R_f = 0.65$ This is close to the expansion parameter $m_{exp} = 2/3$ at the Sedov phase for a supernova shock moving in the medium with the r^{-2} density profile. At first glance this can be interpreted that Cas A is already in the Sedov phase. However this contradicts to the current radius of the reverse shock $R_b \sim 0.6 - 0.7R_f$. Detailed hydrodynamical simulations confirm this qualitative argument. In order to reproduce the current positions of the forward and reverse shocks in Cas A, one has to assume for the forward shock velocity $V_f = 5600$ km s^{-1} (e.g. Chevalier & Oshi 2003; Patnaude & Fesen 2009). This is close to the value $V_f = 5700$ km s^{-1} found in our leptonic model calculations and

Table 3: Secular decrease of electromagnetic radiation, % yr^{-1}

model	1.4GHz	5 keV	1 GeV	1 TeV
H1	0.85	1.14	0.70	0.82
H2	0.53	0.77	0.35	0.47
L1	0.73	0.91	0.14	0.12

is 15% higher than the proper motion $V_f = 4900$ km s^{-1} of X-ray filaments.

Patnaude and Fesen (2009) proposed an explanation of this discrepancy assuming that the forward shock is modified by the cosmic ray pressure. Then the highest energy particles leave the remnant and take away some part of energy. This results in a smaller shock velocity. However, this scenario is possible only if the number density of the circumstellar medium and the ejecta mass are several times lower compared to the parameters $n_H \sim 1$ cm $^{-3}$ and $M_{ej} \sim 2 - 4M_\odot$ derived from X-ray observations. For number density $n_H \sim 1$ cm $^{-3}$ assumed by Patnaude & Fesen, the gamma-ray flux form the pion decay would be a factor of 10 higher in comparison to the one measured by *Fermi* LAT at GeV energies and a factor of 30 higher than the flux of TeV gamma-rays measured by HEGRA, MAGIC and VERITAS.

The lower number densities are indeed used in our models H1 and H2 with an efficient cosmic ray acceleration. However strong magnetic fields assumed results in the steep spectra of accelerated particles. That is why the energy flux of escaped particles is low and does not produce any effect on the forward shock velocity.

An alternative way to resolve the problem would be a deviation from the r^{-2} density profile. The Cas A progenitor might emit fast and tenuous wind prior the explosion and produce a bubble of rarefied gas and a shell of compressed RSG wind in its vicinity. In our hadronic scenario, the collision of the forward shock with this shell results in a significant transfer of the explosion energy to the reverse shock. Correspondingly, the energy related to the forward shock will be reduced leading to a lower speed of the forward shock. Our calculations show that in this way one can bring the forward shock speed in accordance with measurements for the shell radius $R_s = 1.8$ pc. On the other hand, for this shell radius the reverse shock radius appears too large compared to observations. In our modeling we adopt an ad-hoc (smaller) shell radius, $R_s = 1.5$ pc. In this regard we should note that it is possible to reproduce both the measured shock speed and the reverse shock radius for higher stellar wind densities. A similar conclusion has been made by van Veelen et al. (2009) who investigated the impact of a possible Wolf-Rayet phase for the Cas A progenitor on the SNR evolution.

Severe constrains on the radius of the RSG shell have been found by Schure et al. (2008). They showed that the jet observed in Cas A can not pass through the RSG shell if its radius $R_s \geq 0.3 - 0.4$ pc. However the stellar wind density in our model H1 is a factor of 3 lower than the stellar wind density assumed by Schure et al. (2008). Therefore the jet can survive even for larger size of the bubble.

The earlier proper motion measurements by Delaney and Rudnick (2003) is in a good agreement with the forward shock speed derived from our model calculations. However one should note that the results of Delaney and Rudnick (2003) imply $15-20\%$ larger speeds of X-ray filaments than the ones reported by Patnaude and Fesen (2009) (see Table 1 of Patnaude and Fesen 2009). The reason of the discrepancy remains unclear.

Finally, the low measured velocity of X-ray filaments may be related with density disturbances in the circumstellar medium when we observe the brightest X-ray filaments which are formed in the regions with a higher stellar wind density and a correspondingly lower local shock speed. This scenario can be checked easily. Patnaude & Fesen (2009) reported the increase of the brightness of the outer X-ray filament in the north-east periphery of Cas A. The measured value of its speed is $\sim$ 5000 km s^{-1}. Probably the forward shock recently has entered a denser region in this position and initiated an increase of the X-ray brightness. After the shock exits this high density region and enters a lower density region, in future we will observe a decrease of the X-ray brightness and increase of the filament speed. Taking into account that the speeds of different forward shock filaments show a significant scatter 1600 km s^{-1} (see the earlier measurements of Delaney & Rudnick 2003) this scenario seems rather plausible.

We should note that our estimate of the stellar wind mass $2.7M_\odot$ swept up by the forward shock in the hadronic model H1 is several times smaller than the estimate $9M_\odot$ of Vink et al. (1996). However, as indicated in Sect. 4, the fraction of thermal X-rays produced in the shocked circumstellar medium of Cas A is rather uncertain. For example Favata et al. (1997), after subtraction of the non-thermal fraction of X-ray emission, derived $5M_\odot$ of swept up material in Cas A which is

closer to our estimate.

Lee et al. (2013) recently reported the observation of thermal X-rays produced in the shocked circumstellar gas beyond the non-thermal X-ray filaments of Cas A. According to their explanation this X-ray emission is produced at the outlaying parts of the forward shock where CR acceleration is not effective. They also estimated the stellar wind density and derived $6M_\odot$ of the wind material swept up by the forward shock. In our opinion, it is more natural to relate the thermal X-ray emission to the strong gas heating in the upstream regions of the forward shock. The Alfvén velocity is of the order of 1000 km s^{-1} in this region (see Section 8.3 below). The corresponding magnetic amplification is produced by the plasma motions with similar velocities of the gas. These motions unavoidably produce multiple small-scale shocks and the gas heating in the upstream region. It is known that the development of the non-resonant streaming instability results in the magnetic amplification and in the very complex density structure when the main part of the volume is filled with almost empty gas cavities. The cavities are separated by the walls with a denser gas (see e.g. Bell 2004). Therefore mean plasma density derived from X-ray observations can be significantly overestimated.

As for the thermal X-rays produced by ejecta, the flux of thermal X-rays is underproduced in our model H1 (see Section 5). The enhancement factor $\xi_X = 5$ assumed to reproduce the soft X-ray data may be used to estimate the properties of X-ray emitting knots. The number density of nucleons n in the X-ray emitting plasma is estimated as $n \sim n_b V_k^2/V_{be}^2$, where V_k is the shock speed in the knot, V_{be} is the reverse shock speed in the frame of ejecta, and n_b is the mean density of the shocked ejecta. In the model H1 we have $V_{be} = 4.2 \cdot 10^3$ km s^{-1}, while the shock speeds in the X-ray emitting knots are of the order of 800 km s^{-1}. This gives $n \sim 30 n_b$. Then the volume factor of the X-ray emitting plasma must be $\sim 1/180$ in order to reproduce the enhancement factor $\xi_X = 5$. The X-ray emitting plasma contains $\sim 1/6$ of the shocked ejecta mass. Using $n_b \sim 4$ cm^{-3} in the model H1, we estimate the nucleon number density of the X-ray emitting plasma $n \sim 120$ cm^{-3}. The corresponding electron number density $n_e \sim n/2 = 60$ cm^{-3} appears to be in agreement with the results of Lazendic et al. (2006). The measured mean ionization age $n_e\tau \sim 2 \cdot 10^{11}$ cm^{-3} s (Lazendic et al. 2006, Hwang & Laming 2012) then corresponds to the age of the X-ray emitting plasma $\tau \sim 100$ years.

In the model H1, the ram pressure of the stellar wind is $\rho_0 u_w^2 \sim 3.7 \cdot 10^{-12}$ erg cm^{-3}. This value is comparable with the pressure of the interstellar medium. It is expected that the RSG wind is embedded in the rarefied bubble created by the fast wind of Cas A progenitor at the main sequence stage. The gas in the bubble is probably in the pressure equilibrium with the interstellar medium. Then the RSG wind is terminated somewhere not far from the current forward shock position. This occurs at distances $3.5 - 5$ pc for a range of interstellar pressures $1 - 2 \cdot 10^{-12}$ erg cm^{-3}.

The stellar wind gas is compressed and forms a dense outer shell (see modeling of Pérez-Rendón et al. 2009). The forward shock of Cas A will encounter this shell in future. The expected mass of RSG wind material beyond the current forward shock position including the outer RSG shell cannot be less than $5M_\odot$. Another high density shell with mass $\sim 10^4 M_\odot$ forms the walls of the rarefied bubble at distances several tens of parsecs (Pérez-Rendón et al. 2009). Some gas shells are indeed observed in infrared in the vicinity of Cas A (Barlow et al. 2010).

Both shells are considered as perspective targets for gamma-ray production by the highest energy protons escaping SNR Cas A. These protons had no time to travel far from the SNR because even a rectangular propagation at 300 years corresponds to 100 pc distance. Probably they are captured by tangled magnetic fields in the bubble walls.

8.2. Comparison of hadronic and leptonic models

The gamma-emission calculated in the hadronic model H1 is in reasonably good agreement with measurements (see Figure 6). The steepening of the gamma-ray spectrum at TeV energies is achieved by assuming faster diffusion of highest energy particles in accordance with Eq.(4). This assumption affects only the diffusion of highest energy protons and nuclei, but does not have a strong impact on electrons; below the maximum

energy of electrons around 10-20 TeV determined by synchrotron losses (see Figure 3) the diffusion is still close to the Bohm limit. The adjusted values of momenta $P_f = 0.9$, $P_b = 9$ TeV/c which separate two regimes of diffusion can be neither increased nor decreased. The increase of $P_{f,b}$ will lead to contradiction with TeV gamma-ray data, while the decrease of $P_{f,b}$ will contradict to hard X-ray data. Thus we can conclude that the TeV gamma-ray and hard X-ray emission components are produced by particles scattered by small-scale magnetic inhomogeneities (see Eq. (4)).

Diffusion coefficient corresponding to the scattering by small-scale magnetic inhomogeneities is estimated as $D = vkr_g^2/3$. Here $r_g = pc/qB$ is the gyroradius of a charged particle calculated in the small-scale random magnetic field with the square root of the mean square B, k is the inverse scale of the random field. If the magnetic field is amplified in the course of the non-resonant streaming instability, then $k = \gamma/v_A$ (Bell 2004). Here γ is the increment of the instability and v_A is the Alfvén velocity calculated in the non-amplified magnetic field. Comparing the diffusion coefficient with Eq.(4), one finds $P_f = \eta_B qBv_A/c\gamma$. We may estimate the increment of the instability as $\gamma \sim 10\ t^{-1}$ where t is the age of the SNR. The value of the amplified field at the forward shock is $B = V_f\sqrt{4\pi\rho_0}/M_A^f$ (cf. Eq. (3)). Finally we obtain

$$cP_f = \frac{\eta_B qBv_A}{\gamma} \sim \frac{\eta_B qV_f tB_0}{10M_f^A} =$$

$$95\ \text{TeV}\ \eta_B \frac{t_{\rm kyr}B_{0,\mu\rm G}}{M_A^f}\left(\frac{V_f}{10^3\text{km s}^{-1}}\right) \qquad (8)$$

Here B_0 is the magnetic field in the stellar wind. For the forward shock $M_A^f = 4.5$, $V_f = 5.8\cdot10^3$ km s^{-1} and the adjusted value of P_f corresponds to the magnetic field strength in the RSG stellar wind $B_0 = 0.012\mu$G. It corresponds to the magnetosonic Mach number of the wind $M_w = u_w/v_A \sim 570$, while the upper limit $\sim 7\mu$G corresponds to the condition $M_w = 1$. In reality, the stellar wind with an azimuthal magnetic field and $M_w < 5$ is collimated close to the parent star. Since the forward shock in Cas A is rather circular, we conclude that the wind collimation does not occur and the magnetosonic Mach number $M_w > 5$. Then our estimate of the wind magnetic field seems reasonable. The scale of the amplified magnetic field is only $k^{-1} = v_A/\gamma \sim 10^{13}$cm, i.e. 10^{-6} fraction of the remnant radius. It is comparable with the gyroradius of TeV protons calculated in the amplified magnetic field.

Using the estimate of the obtained magnetic field, we can estimate the magnetic field of the Cas A progenitor $B_p = B_0R_fu_w/\Omega R_p^2$ where Ω is the rate of stellar rotation and R_p is the radius of the progenitor. For characteristic values $R_p = 10^{13}$ cm and $\Omega = 10^{-8}$ s^{-1} we obtain $B_p \sim 0.2$ G. This number is significantly below than the value $B_p \sim 0.1 - 1$ kG inferred from observations of H_2O masers at distances $\sim 10^{15}$ cm from several RSGs with powerful stellar winds (Vlemmings et al. 2005). However, it is not excluded that the strong magnetic fields of RSG progenitor dissipate at large distances in the stellar wind e.g. via magnetic reconnection.

We can use the expression similar to Eq. (8) also for the reverse shock. Substituting the reverse shock speed in the ejecta frame, $V_{be} \sim 4.2\cdot10^3$ km s^{-1}, and $M_A^b = 8$ we find the magnetic field in ejecta $B_{ej} \sim 0.3\mu$G.

The maximum energy of protons ~ 40 TeV in the hadronic model H1 is in agreement with previous estimates of maximum energies attainable at fast shocks with non-resonant streaming instability (Zirakashvili & Ptuskin 2008, Bell et al. 2013).

Probably the obtained low value of the strength of the magnetic field in the stellar wind implies that the stellar wind is not a good place for acceleration of cosmic rays up to PeV energies. If the forward shock of Cas A would propagate in the interstellar medium with the magnetic field strength $\sim 5\ \mu$G, the current value of the maximum energy would be a factor of $\sqrt{400}$ higher, namely 800 TeV.

Generally, the high-energy part of the observed spectrum is well reproduced in the leptonic model L1 (see Figure 8). However the low energy part of the spectrum below 1 GeV contributed by non-thermal bremsstrahlung of electrons, does not agree with *Fermi* LAT data.

To avoid overproduction of the non-thermal bremsstrahlung, in the hadronic model H1 we assume that the magnetic field at the reverse shock is rather large. It is interesting that this is possible only due to the presence of the RSG shell. As

mentioned in Section 8.1, this shell results in an effective transfer of the explosion energy in the reverse shock region and in a stronger magnetic field. Because of the lack of such a shell in the hadronic model H2, the energetics of the reverse shock is low, and the magnetic field is rather weak. Therefore, the number of relativistic electrons must be very high to reproduce the radio flux observed from the reverse shock. Then, the non-thermal bremsstrahlung produced by same electrons might significantly exceed the gamma-ray flux observed at sub-GeV energies (see Figure 7).

8.3. Amplification of magnetic field and maximum energies of accelerated particles

The hadronic models demand strong amplification of the magnetic field in order to reproduce the shape of the observed broad-band energy spectra of gamma-rays. For the model H1, the required upstream values are 0.4 mG and 0.2 mG for the forward and reverse shocks, respectively. The Alfvén drift in such fields may lead to steepening of the energy spectra of accelerated particles. This effect has been earlier recognized and explored by Ellison et al. (1999) for Cas A, and recently also by Morlino and Caprioli (2012) for Tycho.

The comparison of the magnetic fields in the stellar wind and ejecta implies very large amplification factors: $3 \cdot 10^4$ and 700 for the forward and reverse shocks, respectively. The magnetic field of the ejecta is the field of the exploded supernova progenitor. Presumably, the field was additionally amplified during the propagation of the radiative shock inside the exploded star when vortex motions downstream of the shock result in the efficient gas mixing (see the modeling of Iwamoto et al. 1997). These motions can also amplify random magnetic fields in the star interior. The random magnetic field may be amplified downstream of the shock moving in the medium with density perturbations (Giacalone & Jokipii 2007). Eventually the shock crosses the outer layers of the exploded star and enters into a circumstellar medium. The downstream material forms a supernova ejecta.

In order to estimate the ejecta random magnetic field in this scenario, let us assume that a small fraction ξ_B of a supernova mechanical energy E_{SN} is transformed into a magnetic energy. At later epochs the magnetic field strength drops proportional to $R_p^2/V_{ej}^2 t^2$, where R_p is the radius of a progenitor and $V_{ej} \sim (2E_{SN}/M_{ej})^{1/2}$ is the characteristic velocity of ejecta. Hence the magnetic field of ejecta at time t is determined as

$$B_{ej} = \frac{M_{ej}}{t^2}\sqrt{\frac{3\xi_B R_p}{2E_{SN}}} =$$

$$0.25\mu\mathrm{G}\xi_B^{1/2}\frac{M_{ej}}{M_\odot}\left(\frac{E_{SN}}{10^{51}\mathrm{erg}}\right)^{-1/2}\left(\frac{R_p}{10^{13}\mathrm{cm}}\right)^{1/2} t_{\mathrm{kyr}}^{-2}. \quad (9)$$

Even for the modest value of $\xi_B = 0.01$ the magnetic field in the ejecta of a core collapse supernovae at $t < 10^3$ yr achieves μG level. Lower values $B_{ej} \sim 10^{-9} - 10^{-8}$G are expected for Ia supernovae originating from a thermonuclear explosion of a white dwarf with a characteristic radius $R_p \sim 10^9$ cm.

In the case of Cas A, we obtain the magnetic field of ejecta ~ 0.5 μG which is close to the value found in the previous Section. Although this field is random, it has a rather large scales, namely an order of 1/100 of the radius of the reverse shock. It can be considered as a large scale field because the non-resonant streaming instability amplifies magnetic fields with even smaller scales.

We should note that the above amplification factors are significantly larger compared to the results obtained from the numerical modeling of nonresonant streaming instability (Zirakashvili & Ptuskin 2008). To a large extent this is not a surprise; it is difficult to amplify the magnetic field by three orders of magnitude in MHD modeling with its limited spatial resolution. It is likely that the amplified magnetic fields are strongly underestimated in the available numerical simulations because of the numerical viscosity.

Another possibility can be related to a possible additional amplification that takes place in the upstream regions of CR modified shocks moving in the medium with strong density perturbations. The deceleration of gas clumps by the CR pressure is slower compared to a less dense plasma. They will stretch and additionally amplify the random magnetic field pre-amplified far upstream of the shock by the non-resonant streaming instability. The possibility of this kind of magnetic amplification was demonstrated recently by Drury and Downes (2012). A similar idea was also proposed earlier by Beresnyak et al. (2009). Given

that the stellar winds and ejecta are very clumpy, so this scenario of additional amplification seems quite plausible.

It should be noted that the high magnetic fields found in our modeling are not rare in young supernova remnants. For example Chandra et al. (2004), based on the observed effect of synchrotron aging of radio electrons in the extragalactic IIb SNR 1993J, derived the downstream magnetic field strength between 0.19 G and 0.33 G after 3200 days of the explosion. This value is also in agreement with the synchrotron self-absorption model of Fransson and Björnsson (1998). For comparison, in our hadronic model H2 for Cas A the downstream magnetic field strength is only 0.04 G at the same 3200th day after the explosion.

The upper limit of the maximum energy of accelerated protons at the forward shock is estimated as (see Zirakashvili & Ptuskin 2008)

$$E_m = 21 \text{ TeV } n_H^{1/2} m_{\rm exp} R_{f,pc} \ln^{-1}(B_0/B_b) \times \left(\frac{\eta_{esc}}{0.05}\right) \left(\frac{V_f}{10^3 \text{ km s}^{-1}}\right)^2 . \quad (10)$$

Here $\eta_{esc} = 2F_E/\rho_0 V_f^3$ is the ratio of the energy flux of run-away particles F_E to the flux of kinetic energy $\rho_0 V_f^3/2$, B_b is the strength of the random magnetic field in the circumstellar medium.

This limit corresponds to the situation when the random magnetic field is amplified via the nonresonant streaming instability exponentially in time (see also Bell et al. 2013, Schure & Bell 2013). The instability is driven by the electric current of the highest energy particles.

For estimates, below we use the value of logarithm $\sim$ 10 in the denominator of Eq. (10), and fix the expansion parameter $m_{\rm exp} = 0.7$. The parameter η_{esc} is determined by the energy density of particles ϵ at the end of their spectrum, just before the cut-off. For shocks with compression ratio $\sim$ 4 the parameter η_{esc} is estimated as $\eta_{esc} \sim 0.5\epsilon/\rho_0 V_f^2$. Using Fig.3, we find $\eta_{esc} \sim 0.01$. Then one obtains $E_m \sim 14$ TeV for the forward shock. For the reverse shock we can use an expression similar to Eq. (10). Using Fig. 3 we estimate $\eta_{esc} = 0.05$ and obtain $E_m \sim 30$ TeV for the reverse shock.

From comparison of these numbers with Fig.3 we see that the maximum energies found in the modeling are significantly larger: $\sim$ 40 TeV and $\sim$ 80 TeV for the forward and reverse shocks, respectively (the maximum energy of oxygen ions 40 TeV per nucleon corresponds to the maximum energy 80 TeV for protons).

Since the parameters of our modeling are adjusted to reproduce the multiwavelength observations of Cas A, we conclude that both magnetic amplification and maximum energy of accelerated particles are underestimated by the theory, despite the rather modest maximum energy of about 40 TeV required to explain the spectral points at very high energy gamma-rays.

The reason is the steep energy distribution of accelerated particles derived from the gamma-ray data. This results in a small value of $\eta_{esc} = 0.01$ at the forward shock. The steep particle spectrum itself is explained by the strong magnetic field and correspondingly by the high Alfvén speed upstream the shock. This result found for Cas A has a more general implication; it shows that the strong magnetic field does not necessarily provide higher maximum energy of accelerated particles.

We should note that in the more realistic case of oblique shocks the maximum energy is higher than the one given by Eq. 10. This equation was derived for quasiparallel shocks. Taking this into account we can conclude that maximum energy of particles accelerated in Cas A corresponds to the number density of the highest energy particles (see Eq.10). Both quantities are in agreement with avalable TeV gamma-ray data.

Apparently, despite certain achievements in the treatment of amplification of the magnetic field in young SNRs in general, further development of theory is needed for better understanding this complex phenomenon regarding, in particular, the demand of very large field amplification by a factor of 10^3.

8.4. Electron injection

The problem of electron injection remains one of the poorly understood aspects of the theory of diffusive shock acceleration of particles in SNRs. This general problem becomes especially important in the models of Cas A without a RSG shell (models H2 and L1) which require very high electron-to-nucleon ratio $K_{en}^b > 0.1$ at the reverse

shock. This exceeds significantly the ratio ~ 0.01 observed in CRs. For this reason we invoke the electron (positron) injection from ^{44}Ti decays (Zirakashvili & Aharonian 2011). To our knowledge, no other ideas have been proposed so far which would provide such a high electron-to-nucleon ratio.

Note that the electron injection from ^{44}Ti decay is not required in the model H1 in which $K^b_{en} = 0.004$. Thus, any other electron injection mechanism which can provide this ratio at the reverse shock can be used in the model H1. However, the positrons from ^{44}Ti decays accelerated later by the reverse shock are of certain interest from the point of view of origin of Galactic CR positrons.

The reason of high values of K^b_{en} in the models H2 and L1 is the low energetics of the reverse shock. Correspondingly, the amplified magnetic fields are weak. Thus, to reproduce the radio flux from the reverse shock, one has to assume large number of injected nonthermal electrons.

The forward shock of Cas A propagates in the stellar wind with a r^{-2} density profile. In this environment the energy of the shocked ejecta consists only 1% of the total energy in shocked plasma. The energetics of reverse shocks is higher and is of the order of 10% for SNRs expanding in the uniform medium. It can reach up to 50% for SNRs expanding in the bubbles where plasma density increases towards the walls of the bubble. This is exactly what happened 40 years after explosion in the model H1. The collision of the shock with the RSG shell transfers a significant fraction of the explosion energy into the region of the reverse shock.

As for the electron injection at the forward shock of Cas A, we used a standard approach and prescribed some injection efficiency in models H1 and H2. Because of the low wind density, the amount of suprathermal electrons produced via Compton scattering of gamma-rays from the decay of ^{56}Co appears to be not sufficient for explanation of the radio and X-ray production by the forward shock of Cas A. At first glance one may increase the injection momentum of electrons to reproduce observations. However, any assumption on injection momenta higher than 200-300 MeV/c leads to contradiction with the radio spectrum.

8.5. On the need of acceleration at the reverse shock

While the acceleration of particles by the reverse shock in Cas A seems to be a natural and well justified component in the general picture, it is fair to ask a question whether can we explain the multiwavelength data of Cas A without invoking the contribution of the reverse shock. Formally, the available data do not allow us to give a certain answer to this question.

Note that a nonlinear DSA model without the consideration of the reverse shock has been discussed by Berezhko et al. (2003). Their model contains many components of our models H1 and H2, including the presence of the RSG shell.

In the model H2 almost all non-thermal X-rays are produced at the forward shock while the thermal bremsstrahlung from the reverse shock contributes to X-rays at energies below 10 keV. The production of non-thermal X-ray emission at the reverse shock is a favored option (Uchiyama & Aharonian 2008, Helder & Vink 2008), however it is not yet firmly established. In particular, it has been argued that the non-thermal X-ray filaments in the reverse shock region are in fact the projected filaments and belong to the forward shock (Delaney et al. 2004).

The observed bright radio-ring can also be explained without the electron acceleration at the reverse shock. The development of the Reighley-Taylor instability at the contact discontinuity can result in an additional amplification of magnetic field in the SNR interior (see e.g. the MHD modeling of Jun and Norman 1996), thus the electrons accelerated at the forward shock may produce enhanced synchrotron radio-emission inside the shell of SNR.

So, perhaps one may argue that the major morphological and spectral features of Cas A reported so far, can be addressed, in principle, by the forward shock. On the other hand one may ask another question about the fundamental difference between the reverse and forward shocks in Cas A. Both shocks propagate in the media having a common origin. They are the same stellar material ejected prior to the explosion (the stellar wind) and during the explosion (the supernova ejecta). As argued in Section 8.2, presently the magnetic fields in the wind and ejecta are comparable. The

speeds of both shocks also are similar. Therefore, there is no reason for DSA to operate effectively in the forward shock and be suppressed in the reverse shock. The situation could be quite different for SNRs produced in Ia supernova explosions. The magnetic field of ejecta in these SNRs is significantly lower compared to the interstellar magnetic field (see Section 8.2). Thus only the forward shock can contribute to the very high energy radiation. However, even at such small fields, the reverse shock can accelerate electrons to GeV energies, and thus be a source of radio emission and gamma-ray bremsstrahlung. Such a scenario presumably is realized in the Tycho where non-thermal X-ray emission is not observed in the reverse shock region while we see radio-emission related with the supernova ejecta (Dickel et al. 1991).

8.6. On the origin of radio-knots

One of the distinct features of the reverse shock is the high electron-to-nucleon ratio at the reverse shock, $K_{en}^{b} \sim 0.004 - 0.8$. Since the reverse shock is modified by the pressure of accelerated ions, a significant part of energy goes into accelerated electrons at the reverse shock. In this regard a plasma of the reverse shock have properties similar to properties of bright radio-knots. Atoyan et al. (2000) found that the energy of relativistic electrons in the knots is close to 10^{-3} fraction of the explosion energy. Since a volume factor of the knots is of the order of 10^{-2} it is easy to estimate that the energy density of accelerated electrons in the radio-knots may be comparable with the mean energy density inside the supernova shell. This may be considered as an independent evidence for a common origin of radio-knots and supernova ejecta. In our model the high energy density is explained by the "radioactive" origin of electrons and positrons injected at the reverse shock (Zirakashvili & Aharonian 2011).

In the inner region of Cas A, the sheet-like structures and filaments are observed in the infrared band (Isensee et al. 2010). This material has not yet encountered the reverse shock. These clumpy structures can produce the X-ray, optical and radio-knots knots after the reverse shock passage.

It is expected that the ejecta clumps have a broad range of densities. The clumps with the lowest density contrast move with a velocity close to the the gas velocity just downstream of the reverse shock. This velocity $u \sim 1600$ km s^{-1} in the model H1 (see Fig.2). The corresponding expansion age $T = R_b/u \sim 10^3$ years is close to the measured value of the radio-knots of the bright radio-ring (Tuffs 1986, Anderson & Rudnick 1995). The large-scale expansion of the radio-ring is even slower and is treated as the expansion of the reverse shock with the speed (1160 ± 500) km s^{-1} (Delaney & Rudnick 2003) which is comparable with the reverse shock velocity $V_b = 770$ km s^{-1} in the model H1.

Denser ejecta clumps are less decelerated after the reverse shock crossing and are initially observed as X-ray knots, while the densest clumps are initially observed as optical knots. At later epochs they have entered the region downstream the forward shock. The radio-electrons accelerated during the transition through the reverse shock are still inside the clumps. Alternatively they can be accelerated by internal shocks in the clump. The clumps are eventually destroyed by the shear Kelvin-Helmholz instability. A material and accelerated electrons of clumps are mixed with the plasma of radio-plateau (see discussion and modeling of Anderson et al. 1994). The electrons emit a radio synchrotron radiation in the strong magnetic field downstream of the forward shock. This field probably is additionally amplified by the shear instability. Since the reverse shock is strongly modified by CR pressure, the electron spectra at the reverse shock and in the clumps have concave shape and are steeper at low energies. This results in steep radio-spectra of the reverse shock and knots. The electrons that escape the knots may produce even steeper radio-spectra because of higher magnetic fields and because of an energy dependent propagation as discussed by Atoyan et al. (2000). In addition, the radio-knots near the forward shock are observed with steeper spectra (Anderson & Rudnick 1995). A possible interpretation could be that closer to the forward shock the magnetic field is stronger. Here, the electrons emitting at the given radio frequency have lower energies. Then their concave spectrum results in the steeper spectra of the knots near the forward shock.

This qualitative picture seems in agreement both with theoretical (Berezhko et al. 2003;

Atoyan et al. 2000) and observational conclusions (Anderson & Rudnick 1995, 1996; Delaney & Rudnick 2003).

9. Summary

Below we summarize the main results of study of the present work on the nonlinear diffusive shock acceleration in Cas A, and the related broad-band electromagnetic radiation.

1. The available observational properties of Cas A are better reproduced by the hadronic model H1 when both the forward and reverse shocks significantly contribute to the broad-band emission. The gamma-ray production is strongly dominated by decays of π^0-mesons from interactions of protons (in the forward shock) and ions (in the reverse shock). The contributions of the forward and reverse shocks around 1 TeV are comparable. The reverse shock produces also approximately 50% of the radio, and 90% of the X-ray synchrotron emission of Cas A.

2. The model requires ejected mass of about $M_{ej} = 2M_\odot$ and the explosion energy $E_{SN} = 1.2 \cdot 10^{51}$erg. The forward shock propagates into the stellar wind with the mass-loss rate $\dot{M} \sim 2.2 \cdot 10^{-5} M_\odot (u_w/20 \text{ km s}^{-1})$ yr^{-1}. Magnetic fields required by the model significantly exceeds the strength of the magnetic field allowed by the MHD treatment of the nonresonant streaming instability. Either the current MHD simulations strongly underestimates the strength of the amplified magnetic field, or an additional amplification is needed. A possible mechanism could be related to the clumpiness of ejecta and the circumstellar medium.

3. Another important ingredient of the model H1 is the presence of the dense shell of the compressed red supergiant stellar wind at the distance $R_s = 1.5$ pc from the supernova progenitor. Contrary to the pure stellar wind models H2 and L1, this permits to explain several observational features of Cas A like the fast decrease of the flux of non-thermal X-rays, the dominance of the reverse shock in the production of non-thermal X-rays and the slow expansion rate of the bright radio-ring and radio-knots.

4. The acceleration efficiency in Cas A should be very high. At present 25% of the energy of supernova explosion is transferred into accelerated particles. The previous claims of the low acceleration efficiency have been based on the high gas density derived from X-ray observations. The plasma density has been strongly overestimated because the non-thermal X-ray component was not properly taken into account.

5. The reverse shock of Cas A is modified by the pressure of energetic ions, positrons and electrons. The energy content in accelerated electrons and positrons from radioactive decay of ^{44}Ti is very close to 10^{48} erg or 0.1% of the explosion energy.

6. The maximum energy of accelerated particles in Cas A cannot exceed 100 TeV. This can be related to the weak magnetic field of about $\sim 0.01\mu G$ in the red supergiant stellar wind where the forward shock propagates. Because of this, the scale of the random magnetic field generated by the nonresonant streaming instability is rather small $\sim 10^{13}$ cm. The corresponding to the small-scale scattering p^2 type dependence of the diffusion coefficient is favored by hard X-ray and TeV gamma-ray data.

7. More accurate spectroscopic measurements of the gamma-ray spectrum of Cas A are highly desirable. The measurements at sub GeV and multi-TeV energies will help to better distinguish between the hadronic and leptonic scenarios. In the case of hadronic origin of gamma-ray emission, the spectral shape at multi TeV energies will give an important information about the maximum energies of accelerated particles. It will be also interesting to search gamma-rays from the vicinity of Cas A. The dense gas shells formed by the winds of the Cas A progenitor seems to be ideal targets for production of gamma-rays by highest energy particles which already have left the remnant. These shells, presumably situated at 5-30′ from the center of Cas A, can be considered as potential sources of multi-TeV gamma-rays - presently or in the near future. It depends on whether or not the high energy particles have already reached the shells.

VNZ acknowledge the hospitality of the Max-Planck-Institut für Kernphysik, where the part of this work was carried out. The work of VNZ was also supported by the RFBR grant in Troitsk.

REFERENCES

Abdo, A.A., Ackermann, M., Ajello, M., et al., 2010, ApJ, 710, L92

Acciari, V.A., Aliu, E., Arlen, T., et al., 2010, ApJ, 714, 163

Aharonian, F., Akhperjanian, A., Barrio, J. et al., 2001, A&A, 379, 112

Albert, J., et al., 2007, A&A, 474, 937

Atoyan, A.M., Aharonian, F.A., Tuffs, R.J., & Völk, H.J., 2000, A&A, 355, 211

Anderson, M.C., Rudnick, L., Leppik, P., Perley, R., & Braun, R., 1991, ApJ, 373, 146

Anderson, M.C., Jones, T.W., Tregillis, L., Rudnick, L., & Kang, H., 1994, ApJ, 421, L31

Anderson, M.C., Rudnick, L., 1995, ApJ, 441, 307

Anderson, M.C., Rudnick, L., 1996, ApJ, 456, 234

Ashworth, W.B., 1980, J. Hist. Astron, 11, 1

Axford, W.I., Leer, E., Skadron, G., 1977, Proc. 15th Int. Cosmic Ray Conf., Plovdiv, 90, 937

Baars, J.W.M., Genzel, R., Paulini-Toth, I.I.K., Witzel, A., 1977, A&A, 61, 99

Bamba A., Yamazaki R., Yoshida, T., Terasawa, T., & Koyama K., 2004, ApJ, 621, 793

Bell, A.R., Gull, S.F., & Kenderdine, S., 1975, Nature, 257, 463

Bell, A.R., 1978, MNRAS, 182, 147

Bell, A.R., 2004, MNRAS, 353, 550

Bell, A.R., Schure, K.M., Reville, B., & Giacinti, G., 2013, MNRAS, 431, 415

Beresnyak, A., Jones, T.W., & Lazarian, A., 2009, ApJ, 707, 1541

Berezhko, E.G., Elshin, V.K., Ksenofontov, L.T., 1994, Astropart. Phys. 2, 215

Berezhko, E.G., Pühlhofer, G., & Völk, H.J. 2003, A&A 400, 971

Berezhko, E.G., & Völk, H.J. 2004a, A&A 419, L27

Barlow, M.J., Krause, O., Swinyard., B.M. et al., 2010, A&A, 518, L138

Blandford, R.D., & Ostriker, J.P. 1978, ApJ, 221, L29

Blumenthal, G.R., & Gould, R.J., 1970, Rev. Mod. Phys. 42, 237

Braun, R., Gull S.F, Perley, R.A., 1987, Nature, 327, 395

Borkowsky, K.J., Szywkowiak, A.E., Blondin, J.M., & Sarazin, C.L., 1996, ApJ, 466, 866

Bykov, A.M., Uvarov, Yu.A., & Ellison, D., 2008, ApJ 689, L133

Chandra, P., Ray, A., Bhatnagar, S., 2004, ApJ, 604, L97

Chevalier, R., 1982, ApJ, 258, 790

Chevalier, R., & Oshi, G., 2003, ApJ, 593, L23

Chevalier, R., 2005, ApJ, 619, 839

Chevalier, R. & Fransson, C., 2006, ApJ 651, 381

Chevalier, R. & Liang, E.P., 1989, ApJ 344, 332

DeLaney, T., & Rudnick, L., 2003, ApJ, 589, 818

DeLaney, T., Rudnick, L., Fesen, R.A. et al., 2004, ApJ, 613, 343

Drury, L.O'C., & Downes, T.P., 2012, MNRAS, 427, 2308

Dickel, J.R., van Breugel, W.J.M., & Strom, R.G., 1991, AJ, 101, 2151

Dolginov, A.Z., & Toptygin, I.N. 1967, JETP, 24, 1195

Ellison, D.C., Ramaty, R., & Jones, F.C., 1990, Proc. 21st ICRC 4, 68

Ellison, D., Decourchelle, A., & Ballet, J., 2005, A&A 429, 569

Ellison, D.C., Goret, F., Baring, M.G., Grenier, I.A., & Lagage P.-O., 1999, Proc. 26th ICRC, Salt Lake City, USA, 3, 468

Fabian, A.C., Willingale, R., Pye, J.P., Murray, S.S., & Fabbiano, G., 1980, MNRAS, 193, 175

Favata, F., Vink, J., Dal Flume, D., et al., 1997, A&A, 324, L49

Fesen, R.A., Becker, R.H., & Goodrich, R.W., 1988, ApJ, 329, L89

Fransson, C., Lundqvist, P., & Chevalier, R., 1996, ApJ, 461, 993

Fransson, C., & Björnsson, C.-I., 1998, ApJ, 509, 861

Giacalone J., & Jokipii J.R., 2007, ApJ, 663, L41

Gotthelf, E.V., Koralesky, B., Rudnick, L., Jones, T.W., Hwang, U., & Petre, R., 2001, ApJ, 552, L39

Gregory, C., 2012, A&A, 538, L8

Helder, E.A., & Vink, J., 2008, ApJ 686, 1094

Hinton, J.,A., & Hofmann, W., 2009, Ann.ReV. Astron. Astrophys., 47, 523

Hughes, J.P., Rakowsky, C.E., Burrows, D.N., & Slane, P.O., 2000, ApJ, 528, L109

Hwang, U., & Laming, J.M., 2003, ApJ, 597, 362

Hwang, U., & Laming, J.M., 2009, ApJ, 703, 883

Hwang, U., & Laming, J.M., 2012, ApJ, 746, 130

Immler, S., Aschenbach, B., & Wang, Q.D., ApJ, 561, L107

Iwamoto, K., Young, T.R., Nakasato, N. et al., 1997, ApJ, 477, 865

Isensee, K., Rudnick, L., & Delaney, T., 2010, ApJ, 725, 2059

Jun, B., & Norman, M.L., 1996, ApJ 465, 800

Kassim, N.E., Perley, L.A., Dwarakamath, K.S., & Erickson, W.C., 1995, ApJ, 455, L59

Kelner, S.R., Aharonian, F.A., & Bugayov, V.V., 2006, Phys. Rev. D, 74, 034018

Kang, H., Jones, T.W., 2006, Astropart. Phys. 25, 246

Kirk, J.G., Duffy, P., & Ball, L., 1995, A&A, 293, L37

Krause, O., Birkmann, S.M., Usada T. et al. 2008, Science, 320, 1195

Krymsky, G.F. 1977, Soviet Physics-Doklady, 22, 327

Lazendic, J.S., Dewey, D., Schulz, N.S., & Canizares, C.R., 2006, ApJ, 651, 250

Lagage, P.O., & Cesarsky, C.J., 1983, A&A, 125, 249

Laming, J.M., & Hwang, U., 2003, ApJ, 597, 347

Lee, J.J., Paok, S., Hughes, J.P., & Slane, P.O., 2013, arXiv:1304.3973

Malkov, M.A., & Drury, L.O'C, 2001, Reports on Progress in Physics, 64, 429

Markert, T.H., Clark, G.W., Winkler, P.F., & Canizares, C.R., 1983, ApJ, 268, 134

Maeda, Y., Uchiyama, Y., Bamba, A., et al., 2009, PASJ, 61, 121

Mauron, N., & Josselin, M., 2011, A&A, 526, A156

McKenzie, J.F., & Völk, H.J., 1982, A&A, 116, 191

Mori, M., 2009, Astropart. Phys., 31, 341

Morlino, G., & Caprioli, D., 2012, A&A, 538, 15

Morlino, G., 2012, MNRAS, 412, 2333

Morse, J.A., Fesen, R.A., Chevalier, R. et al., 2004, ApJ, 614, 727

O'Sullivan, C., & Green, D.A., 1999, MNRAS, 303, 575

Patnaude, D.J., & Fesen, R.A., 2009, ApJ, 697, 535

Patnaude, D.J., Vink,J., Laming, J.M.,& Fesen, R.A., 2011, ApJ, 729, 28

Pérez-Rendón, B., García-Segura, G., & Langer, N., 2009, A&A, 506,1249

Ptuskin, V.S., Zirakashvili, V.N., & Seo, E.S., 2010, ApJ

Reed, J.E., Hester, J.J., Fabian, A.C., & Winkler, P.F., 1995, ApJ, 440, 706

Renaud, M., et al., 2006, ApJ, 647, L41

Rieger, F., de Oña Wilhelmi, E., & Aharonian, F., 2013, Frontiers of Physics, in press

Reynoso, E.M., Goss, W.M., Dubner, G.M., Winkler, P.F., & Schwarz, U.J., 1997, A&A, 317, 203

Schure, K.M., Vink, J., García-Segura, G., & Achterberg, A., 2008, ApJ, 686, 399

Schure, K.M., Bell, A.R., Drury, L.O'C., & Bykov, A.M., 2012, Space Science Rev., 173, 491

Schure, K.M., & Bell, A.R., arXiv:1307.6575

Spitzer, L. 1968, Diffuse matter in space (New York: Intersience)

Tatischeff, V., 2009, A&A, 499, 191

Tuffs, R.J., 1986, MNRAS, 219, 13

Uchiyama, Y., & Aharonian, F.A., 2008, ApJ, 677, L105

van Veelen, B., Langer, N., Vink J., Garcia-Segura G., & van Marle A.J., 2009, A&A, 503, 495

Vink, J., Kaastra, J.S., & Bleecker, J.A.M., 1996, A&A, 307, L41

Vink, J., et al., 2001, ApJ, 560, L79

Vlemmings, W.H.T., van Langevelde, H.J., & Diamond, P.J., 2005, A&A 434, 1029

Völk, H.J., Berezhko, E.G., & Ksenofontov, L.T., 2003, A&A, 409, 563

Völk, H.J., Berezhko, E.G., & Ksenofontov, L.T., 2005, A&A, 433, 229

Weiler, K.W., Williams, C.L., Panagia, N., Stockdale, C.J., et al., 2007, ApJ, 671, 1959

Willingale, R., Bleecker, J.A.M., van der Heiden, K.J., Kaastra, J.S., & Vink, J., 2002, A&A, 381, 1039

Willingale, R., Bleecker, J.A.M., van der Heiden, K.J., & Kaastra, J.S., 2003, A&A, 398, 1021

Yang, R.-Z., Sahakyan, N., de Ona Whilhelmi, E., Aharonian, F., & Rieger, F., 2012, A&A, 542, A19

Zirakashvili, V.N. 2007, A&A 466, 1

Zirakashvili, V.N., Ptuskin, V.S., 2008, ApJ 678, 939

Zirakashvili, V.N., & Aharonian, F.A., 2010, ApJ, 708, 965

Zirakashvili, V.N., & Aharonian, F.A., 2011, Phys. Rev. D, 84, 083010

Zirakashvili, V.N., Ptuskin, V.S., 2012, Astropart. Phys., 39, 12

This 2-column preprint was prepared with the AAS LaTeX macros v5.2.